nature immunology

ARTICLES

https://doi.org/10.1038/s41590-019-0584-x

Environmental cues regulate epigenetic reprogramming of airway-resident memory CD8$^+$ T cells

Sarah L. Hayward[1,4], Christopher D. Scharer[1,4], Emily K. Cartwright[1], Shiki Takamura[2], Zheng-Rong Tiger Li[1], Jeremy M. Boss[1] and Jacob E. Kohlmeier[1,3*]

Tissue-resident memory T cells (T_{RM} cells) are critical for cellular immunity to respiratory pathogens and reside in both the airways and the interstitium. In the present study, we found that the airway environment drove transcriptional and epigenetic changes that specifically regulated the cytolytic functions of airway T_{RM} cells and promoted apoptosis due to amino acid starvation and activation of the integrated stress response. Comparison of airway T_{RM} cells and splenic effector-memory T cells transferred into the airways indicated that the environment was necessary to activate these pathways, but did not induce T_{RM} cell lineage reprogramming. Importantly, activation of the integrated stress response was reversed in airway T_{RM} cells placed in a nutrient-rich environment. Our data defined the genetic programs of distinct lung T_{RM} cell populations and show that local environmental cues altered airway T_{RM} cells to limit cytolytic function and promote cell death, which ultimately leads to fewer T_{RM} cells in the lung.

T_{RM} cells act as sentinels of the immune system within peripheral tissues and are uniquely positioned to rapidly recognize and respond to invading pathogens[1–3]. T_{RM} cells share many properties with effector-memory T cells (T_{EM} cells), including genetic architecture poised for cytokine production and robust cytolytic activity[2,4]. Despite these functional similarities, T_{RM} cells are defined by a unique core transcriptional signature that supports long-term tissue residence through the regulation of cell-trafficking molecules and adaptations that enable survival in the tissue microenvironment[5,6]. These adaptations allow for long-term protection by T_{RM} cells in sites such as the skin and gut, where they can provide almost sterilizing immunity when present in sufficient numbers[1,3]. In contrast, the efficacy of cellular immunity against respiratory pathogens gradually wanes, and this decline is associated with the progressive loss of virus-specific T_{RM} cells in the lung[7,8]. However, the mechanisms driving the transient nature of lung T_{RM} cells are not well defined.

After clearance of a primary influenza infection, virus-specific memory CD8$^+$ T cells are localized to secondary lymphoid organs and peripheral tissues, primarily the lung interstitium and the lung airways[9–11]. Evidence from animal models and humans indicates that memory CD8$^+$ T cells confer protective immunity to respiratory viruses by substantially decreasing viral loads, limiting immunopathology and lowering disease burden[7,8,12–14]. The lung CD8$^+$ T_{RM} cell pool comprises two distinct populations: airway T_{RM} (A-T_{RM}) cells and interstitial T_{RM} (I-T_{RM}) cells, with unique functional properties. A-T_{RM} cells are poorly cytolytic compared with I-T_{RM} cells, yet are sufficient to protect against influenza challenge through the rapid production of antiviral cytokines[15]. In addition, the number of A-T_{RM} cells correlates with the efficacy of cellular immune protection in the lung[8]. These findings have raised questions about the requirements for differentiation and maintenance of these distinct populations of lung T_{RM} cells, and about how environmental niches shape the function and lifespan of these cells, but the molecular underpinnings of differences between A-T_{RM} and I-T_{RM} cells have not been explored to date.

Lung T_{RM} cells are gradually lost under steady-state conditions[16]. However, T_{RM} cells in the lung and other barrier tissues have a consistent transcriptional profile, raising questions as to why the lifespan of T_{RM} cells would vary between tissues[6,17–19]. One potential explanation for these conflicting findings is that lung T_{RM} cells have often been investigated as a single population, without separation into A-T_{RM} and I-T_{RM} cell subsets. Given the functional differences between these subsets and the distinct environments where they reside, a detailed comparison of A-T_{RM} and I-T_{RM} cells could be informative about the mechanisms that control their biology and regulate the decline of lung T_{RM} cells.

In the present study, we examined the decline of cellular immunity to the influenza virus over time, with a focus on comparing flu-specific lung T_{RM} cells in the airways and interstitium. We observed that A-T_{RM} and I-T_{RM} subsets were gradually lost due to apoptosis in the tissue, and transcriptome and chromatin accessibility analysis (ATAC) revealed an enrichment of genes in A-T_{RM} cells associated with the integrated stress response (ISR), notably the amino acid starvation pathway. These stress-related programs were due to the airway environment, whereas core T_{RM} signature genes were regulated during the initial differentiation of A-T_{RM} cells after infection. Overall, these findings provide new insight into the role of environmental cues in controlling the differential functions and lifespan of A-T_{RM} and I-T_{RM} cells, and identify pathways that may be manipulated to improve the longevity of cellular immunity against respiratory pathogens.

Results

A-T_{RM} cells rapidly decline after influenza infection. To confirm that cellular immune protection against heterologous influenza challenge is rapidly lost[7,8], C57Bl/6J wild-type mice infected with

[1]Department of Microbiology and Immunology, Emory University School of Medicine, Atlanta, GA, USA. [2]Department of Immunology, Kindai University Faculty of Medicine, Osaka-Sayama, Japan. [3]Emory-UGA Center of Excellence for Influenza Research and Surveillance, Atlanta, GA, USA. [4]These authors contributed equally: Sarah L. Hayward, Christopher D. Scharer. *e-mail: jkohlmeier@emory.edu

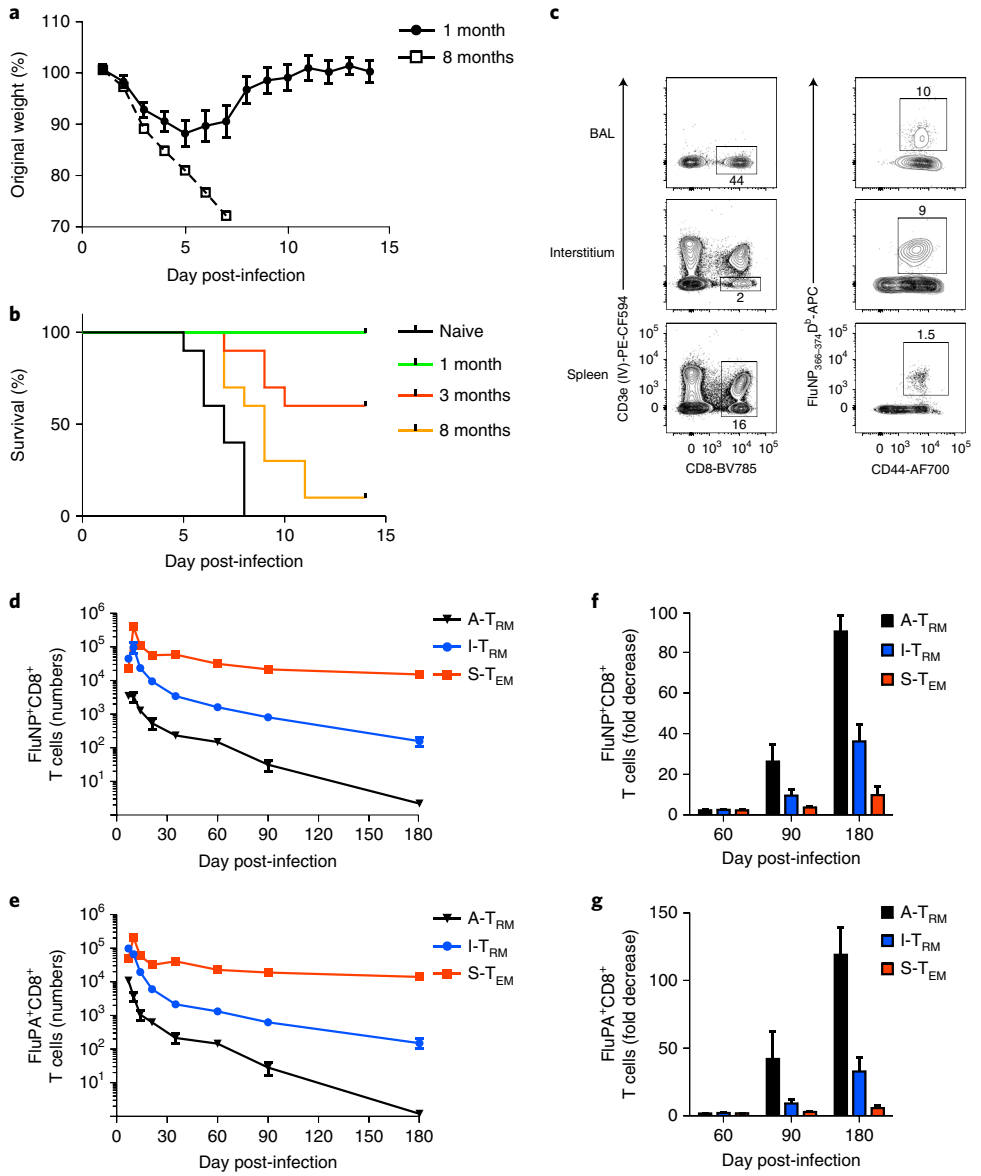

Fig. 1 | Decline of A-T_{RM} and I-T_{RM} cells over time. a, Morbidity curve examining decline of protection in x31-immune mice after heterologous PR8 challenge ($n=20$ per group, combined from two experiments). **b**, Mortality curve examining decline of protection from heterologous challenge over time after a ×10 LD_{50} PR8 challenge ($n=20$ per group, combined from two experiments). **c**, Intravital (IV) staining showing FluNP$^+$CD8$^+$ T cells from BAL, lung interstitium and spleen ($n=5$, representing three experiments). **d**,**e**, The number of FluNP$^+$ (**d**) and FluPA$^+$ (**e**) CD8$^+$ S-T_{EM}, A-T_{RM} or I-T_{RM} cells in wild-type mice at various times post-x31 infection ($n=15$, combined from three experiments). Data are represented as mean ± s.e.m. **f**,**g**, Fold decrease in FluNP$^+$CD8$^+$ T cells (**f**) and FluPA$^+$CD8$^+$ T cells (**g**) from wild-type mice at various times post-x31 infection compared with the number of FluNP$^+$CD8$^+$ T cells or FluPA$^+$CD8$^+$ T cells at day 35 post-infection ($n=15$, combined from three experiments). Data are represented as the mean ± s.e.m.

influenza A/HKx31 (x31, H3N2) were challenged with influenza A/PR8 (PR8, H1N1) at 1, 3 or 8 months after infection with x31. The PR8-challenged mice showed progressively more weight loss (Fig. 1a) and decreased survival (Fig. 1b) as time from the initial infection with x31 increased. To determine the kinetics of the loss of flu-specific A-T_{RM} and I-T_{RM} cells in the lung, we analyzed the number of influenza nucleoprotein (FluNP)$^+$ and acid polymerase (FluPA)$^+$ CD8$^+$ T cells on days 8, 10, 14, 21, 35, 60, 90 and 180 post-infection in the lung airways (bronchoalveolar lavage (BAL)), lung interstitium and spleen using intravital labeling, which allows for the identification of extravascular T cells in the tissue by gating on IV$^-$CD8$^+$ T cells (negative for staining with the intravital antibody). Tissue-resident, FluNP$^+$, memory CD8$^+$ T cells were present in both the lung airways and the interstitium 35 d post-x31 infection (Fig. 1c). Regardless of specificity, the number of CD8$^+$IV$^-$ A-T_{RM} cells and CD8$^+$IV$^-$ I-T_{RM} cells gradually declined from day 35 to day 180 post-infection, whereas the number of splenic effector, memory CD8$^+$CD62L$^-$ T cells (S-T_{EM}) remained mostly unchanged (Fig. 1d,e). We observed a similar trend after infection with Sendai virus (see Supplementary Fig. 1), indicating that the effect was not specific to influenza virus. A-T_{RM} cells were lost much more rapidly than I-T_{RM} cells, declining almost 100-fold by 6 months post-infection compared with 40-fold for I-T_{RM} cells (Fig. 1f,g). These data indicated that A-T_{RM} and I-T_{RM} cells were lost over 6 months post-infection, with a more accelerated decline of the A-T_{RM} cells.

A-T_{RM} and I-T_{RM} cells do not recirculate and undergo apoptosis. To investigate the mechanisms that contributed to the gradual decline

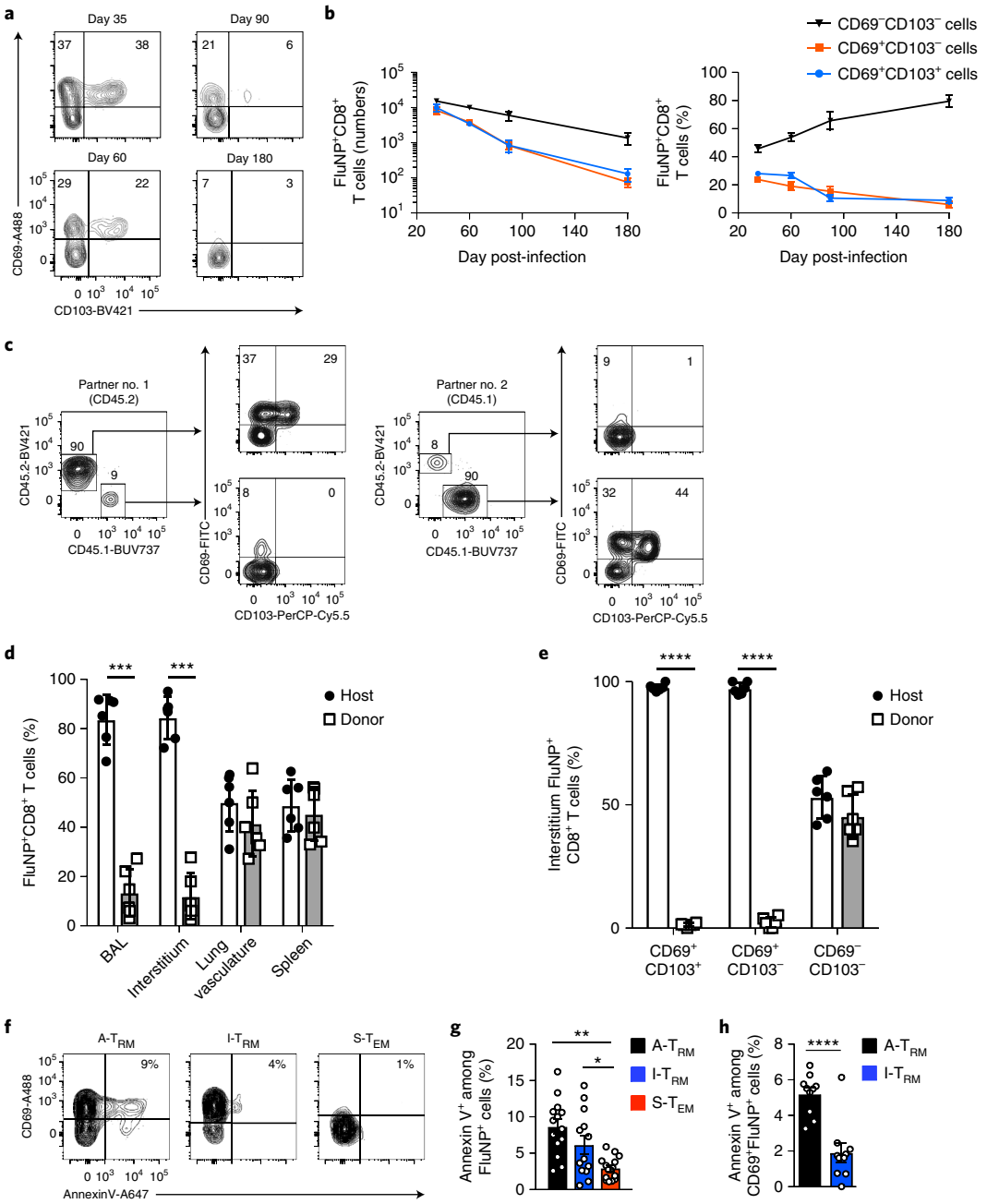

Fig. 2 | In situ apoptosis drives lung T_{RM} cell decline. a, Expression of CD69 and CD103 on FluNP$^+$ I-T_{RM} cells from wild-type mice on days 35, 60, 90 or 180 post-x31 infection. **b**, Number and frequency of CD69$^-$CD103$^-$, CD69$^+$CD103$^-$ and CD69$^+$CD103$^+$ FluNP$^+$ I-T_{RM} cell subsets from mice infected as in **a** ($n=15$, combined from three experiments). Data are represented as the mean ± s.e.m. **c**, Expression of CD69 and CD103 on CD45.2$^+$ or CD45.1$^+$ FluNP$^+$IV$^-$CD8$^+$ lung T_{RM} cells from one parabiont pair 49 d post-x31 infection and 21 d post-parabiosis surgery. **d**, Frequency of CD45.2$^+$ or CD45.1$^+$ FluNP$^+$CD8$^+$ T cells in the BAL, lung interstitium, lung vasculature and spleen of parabiosis partners as in **c** ($n=6$ parabiont pairs, representing two experiments). Data are represented as the mean ± s.e.m. The significance was determined using the paired Student's *t*-test. **e**, Frequency of CD45.2$^+$ or CD45.1$^+$ FluNP$^+$ I-T_{RM} cells from parabiosis partners as in **c**, based on CD69 and CD103 expression ($n=6$ parabiont pairs, representing two experiments). Data are represented as the mean ± s.e.m. The significance was determined using the paired Student's *t*-test. **f**, Expression of annexin V and CD69 on FluNP$^+$ A-T_{RM}, I-T_{RM} or S-T_{EM} cells from wild-type mice 35 d post-infection with x31 ($n=14$, combined from three experiments). **g**, Frequency of AnnexinV$^+$FluNP$^+$ A-T_{RM}, I-T_{RM} or S-T_{EM} cells from wild-type mice 35 d post-infection with x31 ($n=14$, combined from three experiments). Data are represented as the mean ± s.e.m. The significance was determined using the unpaired Student's *t*-test. **h**, Frequency of AnnexinV$^+$ cells among FluNP$^+$CD69$^+$ A-T_{RM} or I-T_{RM} cells as in **g** ($n=10$, combined from two experiments). Data are represented as the mean ± s.e.m. The significance was determined using the unpaired Student's *t*-test. *P* values are as follows: $^*P<0.05$, $^{**}P<0.01$, $^{***}P<0.001$, $^{****}P<0.0001$.

of lung T_{RM} cells, we first examined whether their loss was limited to a subset of the T_{RM} population based on expression of the residency markers CD69 and CD103. The number of CD69$^-$CD103$^-$, CD69$^+$CD103$^-$ and CD69$^+$CD103$^+$ FluNP$^+$ I-T_{RM} cells all declined over 6 months post-influenza infection (Fig. 2a,b). To test whether the gradual loss of circulating CD62L$^-$ T_{EM} cells contributed to the loss of lung T_{RM} cells, we measured the number of S-T_{EM} cells after x31 influenza infection. There was a modest decrease in the number

of FluNP$^+$ S-T_{EM} cells between 1 and 6 months post-infection in wild-type mice (see Supplementary Fig. 2), similar to previous reports[20]. CD69$^+$CD103$^-$ and CD69$^+$CD103$^+$ FluNP$^+$ I-T_{RM} cells declined notably faster than FluNP$^+$ S-T_{EM} cells between 1 and 6 months post-infection (see Supplementary Fig. 2c). In contrast, CD69$^-$CD103$^-$CD8$^+$ FluNP$^+$IV$^-$ T cells in the lung, which were probably transiting T_{EM} cells, declined at the same rate as S-T_{EM} cells (see Supplementary Fig. 2c), indicating that the decline of lung T_{RM} cells did not coincide with the gradual loss of S-T_{EM} cells.

To address whether A-T_{RM} and I-T_{RM} cells were truly resident populations, or whether they were maintained by replenishment from the circulating memory T cell pool, we performed parabiosis in congenic mice, 4 weeks post-infection with x31. Intravascular labeling after 3 weeks of parabiosis indicated that 90% of FluNP$^+$ I-T_{RM} cells were host derived and expressed the tissue residency markers CD69 and CD103 (Fig. 2c), whereas the few partner-derived FluNP$^+$IV$^-$CD8$^+$ T cells were CD69$^-$CD103$^-$ (Fig. 2c), suggesting that they were transiting T_{EM} cells. Comparison across tissues indicated that FluNP$^+$CD8$^+$ T cells from the host and partner were in equilibrium in the spleen and the lung vasculature, but were notably enriched for host-derived cells among FluNP$^+$ A-T_{RM} and I-T_{RM} cells (Fig. 2d). Analysis of CD69 and CD103 expression on FluNP$^+$ I-T_{RM} cells found that >95% of CD69$^+$CD103$^-$ and CD69$^+$CD103$^+$ cells were host derived (Fig. 2e). These observations indicated that lung T_{RM} cells did not exit the tissue and were not replenished by circulating S-T_{EM} cells.

To investigate the possibility that lung T_{RM} cells were lost due to death in the tissue, we examined expression of the proapoptotic marker annexin V on FluNP$^+$ A-T_{RM}, I-T_{RM} and S-T_{EM} cells on day 35 post-infection with x31. A-T_{RM} and I-T_{RM} cells had increased annexin V staining compared with S-T_{EM} cells (Fig. 2f,g), indicating increased apoptosis. We also observed an important increase in AnnexinV$^+$ cells among CD69$^+$ A-T_{RM} cells compared with CD69$^+$ I-T_{RM} cells (Fig. 2h). Thus, the gradual loss of lung T_{RM} cells was due to increased apoptosis within the tissue, and A-T_{RM} cells had a higher rate of cell death compared with I-T_{RM} cells, possibly due to unique microenvironmental effects within the lung on the survival of T_{RM} cells.

A-T_{RM} cells are transcriptionally distinct from I-T_{RM} cells. Next we used RNA sequencing (RNA-seq) to compare the transcriptional profiles of FluNP$^+$IV$^-$CD8$^+$ A-T_{RM} cells, FluNP$^+$IV$^-$CD8$^+$ I-T_{RM} cells and FluNP$^+$CD8$^+$ S-T_{EM} cells isolated by cell sorting (Fig. 3a) from wild-type mice 35 d post-infection with x31. Principal component analysis (PCA) of the 9,362 genes detected indicated that I-T_{RM} cells more closely aligned with S-T_{EM} cells than with A-T_{RM} cells (Fig. 3b). Differentially expressed genes (DEGs) (false discovery rate (FDR) < 0.05, absolute $\log_2$(fold change) ($\log_2$(FC)) > 1) indicated that each population had a distinct expression profile, with A-T_{RM} cells being the most transcriptionally distinct (Fig. 3c). We correlated the change in expression for genes differentially expressed between A-T_{RM} and S-T_{EM} cells, or between A-T_{RM} and I-T_{RM} cells, and identified gene expression changes unique to each comparison (for example, *Itgae*, *Ctla4*), as well as shared differences (for example, *Klrg1*, *Asns*) (Fig. 3d). DEGs upregulated in airway T_{RM} cells included genes involved in amino acid transport (*Slc1a4*, *Slc7a5*) and amino acid synthesis (*Asns*, *Lars*), whereas DEGs shared by A-T_{RM} and I-T_{RM} cells included genes associated with programming of T_{RM} cells (*Itga1*, *Itgae*, *Ahr*) (Fig. 3d). Gene set enrichment analysis (GSEA)[21] identified a notable positive enrichment in genes associated with the unfolded protein response in A-T_{RM} cells compared with both I-T_{RM} and S-T_{EM} cells (Fig. 3e), suggesting stresses unique to the airway and not present in the lung interstitium or spleen. A-T_{RM} cells were also negatively enriched for genes involved in the cytotoxic T lymphocyte (CTL) pathway, including *Prf1*, *Gzma*, *Gzmb* and *Gzmk* (Fig. 3e), which supported previous reports that A-T_{RM} cells are poorly cytolytic[15]. In addition, A-T_{RM} cells showed altered expression of DEGs related to intrinsic cell death, maintenance of cell survival under cell stress and activation of the ISR, including *Dusp1*, *Bax*, *Bcl2*, *Bbc3*, *Pim2* and the proapoptotic transcription factor *Ddit3* (Fig. 3f). However, A-T_{RM} and I-T_{RM} cells shared the expression of a core set of known T_{RM} genes, including *Itgae*, *Cdh1*, *Ahr*, *Cxcr6*, *Klf2* and *S1p1r*[6,18] (Fig. 3f). To confirm the RNA-seq findings, we performed a second analysis using FluNP$^+$CD8$^+$ T cells sorted from three independent cohorts of wild-type mice 35 d after x31 infection, which included FluNP$^+$IV$^+$CD8$^+$ T_{EM} cells from the lung vasculature, in addition to FluNP$^+$ A-T_{RM}, I-T_{RM} and S-T_{EM} cells, to address whether processing of the lung tissue impacted the genetic signature of I-T_{RM} cells. Data from this additional analysis showed a similar pattern of gene expression to the original analysis, and indicated that FluNP$^+$ I-T_{RM} cells and lung vascular T_{EM} cells had unique transcriptional signatures (see Supplementary Fig. 3). In addition, staining for BCL2 protein indicated that BCL2 was notably upregulated in A-T_{RM} cells compared with I-T_{RM} cells (see Supplementary Fig. 4). These data indicated that A-T_{RM} cells had a distinct transcriptional profile, characterized by cellular stress and balancing of pro- and antiapoptotic signals compared with I-T_{RM} cells, and suggested that the local microenvironment had a critical role in regulating T_{RM} cell biology.

A-T_{RM} cell survival and homeostasis are epigenetically regulated. The immediate microenvironment can impact the epigenetic programming and function of immune cells[22], including those in the lung[23]. To determine the effect of T_{RM} cell location on epigenetic programming, we used ATAC-sequencing (ATAC-seq)[24,25] to assess the chromatin accessibility landscape of FluNP$^+$CD8$^+$ A-T_{RM}, I-T_{RM} and S-T_{EM} cells 35 d post-influenza infection. The PCA of 47,683 accessible loci indicated that A-T_{RM} cells clustered separately from I-T_{RM} and S-T_{EM} cells (Fig. 4a). These differences were not due to tissue processing and were consistent in three independent cohorts of wild-type mice that had been infected with x31 35 d earlier (see Supplementary Fig. 3). We identified differentially accessible regions (DARs) (FDR < 0.05, absolute $\log_2$(FC) > 1) between each T_{RM} cell subset (Fig. 4b), and integrated them with the RNA-seq data to determine coordinated changes in the epigenome and transcriptome for each T_{RM} cell subset[26]. Using *k*-means clustering, we observed three distinct patterns (k1–k3) in the data that could be mapped to each of the cell types: k1 in S-T_{EM} cells, k2 in I-T_{RM} cells and k3 in A-T_{RM} cells (Fig. 4c). This analysis indicated that A-T_{RM} cells had a unique chromatin accessibility landscape compared with I-T_{RM} and S-T_{EM} cells, which resulted in coordinated changes in gene expression and suggested that the epigenetic architecture of A-T_{RM} cells may be impacted by their environment.

Next we examined the enrichment of transcription factor DNA-binding motifs within the DARs in patterns k1, k2 and k3. Chromatin accessibility patterns for A-T_{RM}, I-T_{RM} and S-T_{EM} cells were all enriched for motifs for ETS and RUNX (Fig. 4d), which are common to memory CD8$^+$ T cells[27]. The pattern k3, which was enriched in A-T_{RM} cells, was enriched in binding motifs for STAT5 and DDIT3 (Fig. 4d). A-T_{RM} and I-T_{RM} cells shared enrichment for AP-1-binding motifs, whereas I-T_{RM} cells were uniquely enriched for FOS and CREM motifs (Fig. 4d). Analysis of the unique accessibility footprint surrounding CREM, STAT5 and DDIT3 motifs indicated that CREM motifs were highly accessible in I-T_{RM} cells compared with S-T_{EM} and A-T_{RM} cells (Fig. 4e). Similarly, STAT5 and DDIT3 were notably more accessible in A-T_{RM} cells compared with S-T_{EM} and I-T_{RM} cells (Fig. 4e).

To complement the motif analysis, we performed gene ontology (GO) analysis to determine the functional enrichment of the genes in each pattern. The S-T_{EM} pattern (k1) was enriched for genes associated with T cell differentiation and activation (Fig. 4f). The A-T_{RM} pattern (k3) was enriched for genes implicated in cellular homeostasis,

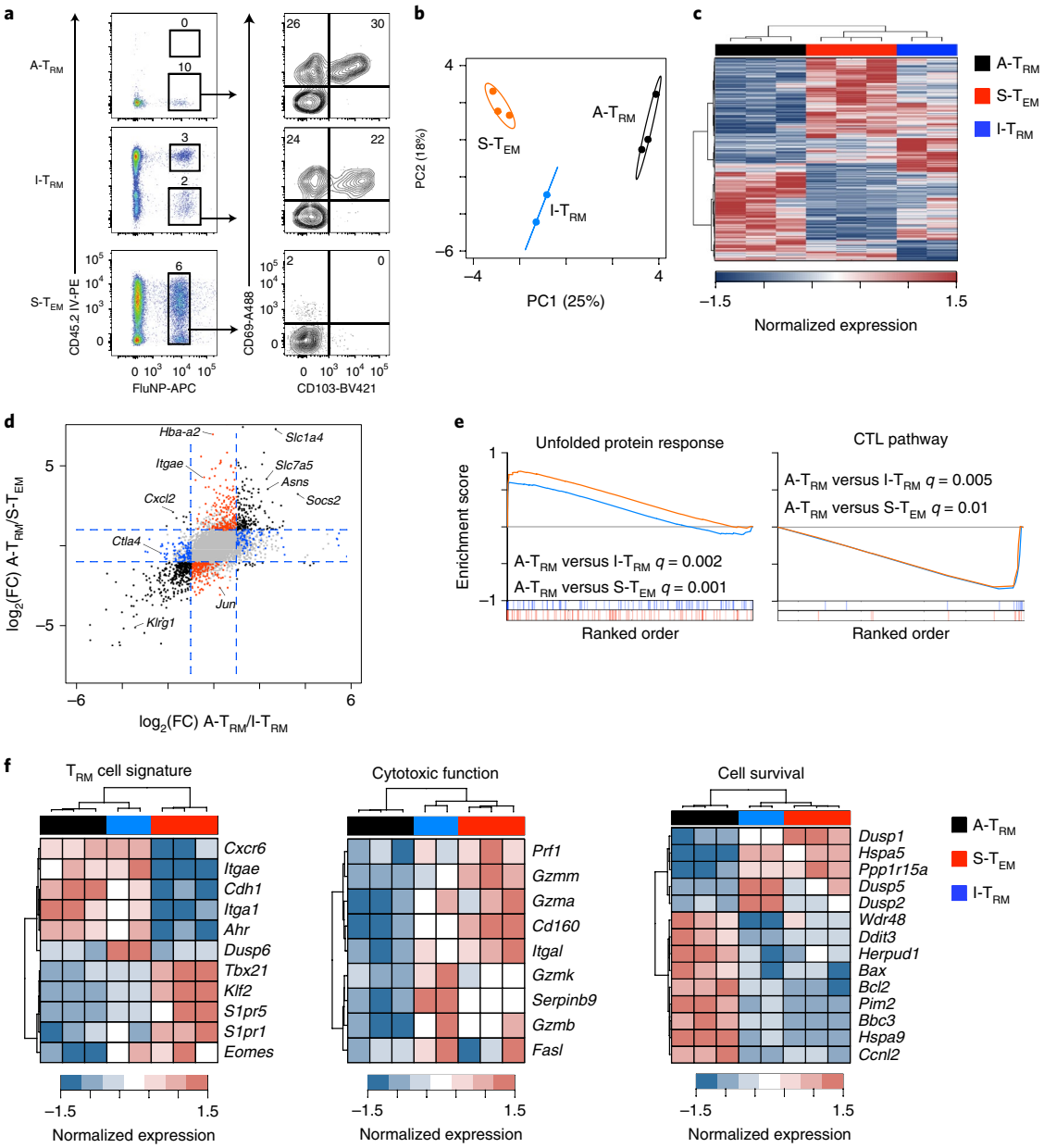

Fig. 3 | Influenza-specific lung A-T$_{RM}$ and I-T$_{RM}$ cells have distinct transcriptional profiles. a, Sorting strategy of FluNP$^+$ A-T$_{RM}$, I-T$_{RM}$ or S-T$_{EM}$ cells from wild-type mice 35 d post-x31 infection for RNA-seq. **b**, PCA of 9,362 detected genes from cells described in **a**. The circles represent 99% confidence intervals. BAL (A-T$_{RM}$, $n=3$), spleen (S-T$_{EM}$, $n=3$) and lung interstitium (I-T$_{RM}$, $n=2$). **c**, Heatmap of 1,622 DEGs from A-T$_{RM}$, I-T$_{RM}$ or S-T$_{EM}$ cells. **d**, Scatterplot of correlation of DEGs between A-T$_{RM}$ and S-T$_{EM}$ cells and between A-T$_{RM}$ and I-T$_{RM}$ cells isolated as in **a**. Black, DEGs in A-T$_{RM}$ cells compared with S-T$_{EM}$ and I-T$_{RM}$ cells; red, DEGs between only A-T$_{RM}$ and S-T$_{EM}$ cells; blue, DEGs between I-T$_{RM}$ and S-T$_{EM}$ cells. **e**, GSEA of the unfolded protein response and CTL pathway gene sets comparing A-T$_{RM}$ cells with I-T$_{RM}$ and S-T$_{EM}$ cells as in **a**. **f**, Heatmap of selected genes derived from **c**, related to a core T$_{RM}$ cell signature, cytotoxic function and cell survival, as in **a**.

endoplasmic reticulum (ER) stress, hypoxia and glucose starvation (Fig. 4f). The extrinsic apoptosis pathway was uniquely enriched in I-T$_{RM}$ cells (k2, Fig. 4f), which might explain the increased apoptosis in these cells compared with S-T$_{EM}$ cells. *Slc7a5* and *Asns*, which encode an amino acid transporter and asparagine synthetase, respectively, contained DARs with increased accessibility and were more highly expressed in A-T$_{RM}$ cells compared with I-T$_{RM}$ and S-T$_{EM}$ cells (Fig. 4g), suggesting differential epigenetic and transcriptional programming of pathways related to cell stress and apoptosis in A-T$_{RM}$ cells. These data suggest that the local environments of the airways and interstitium contribute to differential epigenetic programming in lung T$_{RM}$ cell subsets.

Amino acid starvation controls the lifespan of A-T$_{RM}$ cells. The ISR is activated by several triggers of cellular stress, including viral infection, ER stress and amino acid starvation, with the goal of inhibiting protein translation, and can induce apoptosis if the stress is not resolved[28]. Different stressors activate unique pathways to restore cellular homeostasis[28]. To determine the pathway responsible for the gradual loss of A-T$_{RM}$ cells, we analyzed genes known to be involved in responses to cellular stress that were differentially expressed in A-T$_{RM}$ cells. Most transcripts upregulated in A-T$_{RM}$ cells were involved in amino acid transport (*Slc25a22*, *Slc1a4*, *Slc7a5*), amino acid synthesis (*Mars*, *Lars*, *Sars*, *Aars*, *Asns*), recognition of uncharged transfer RNAs (*Eif2ak4*), cell cycle arrest (*Cdkn1a*) and

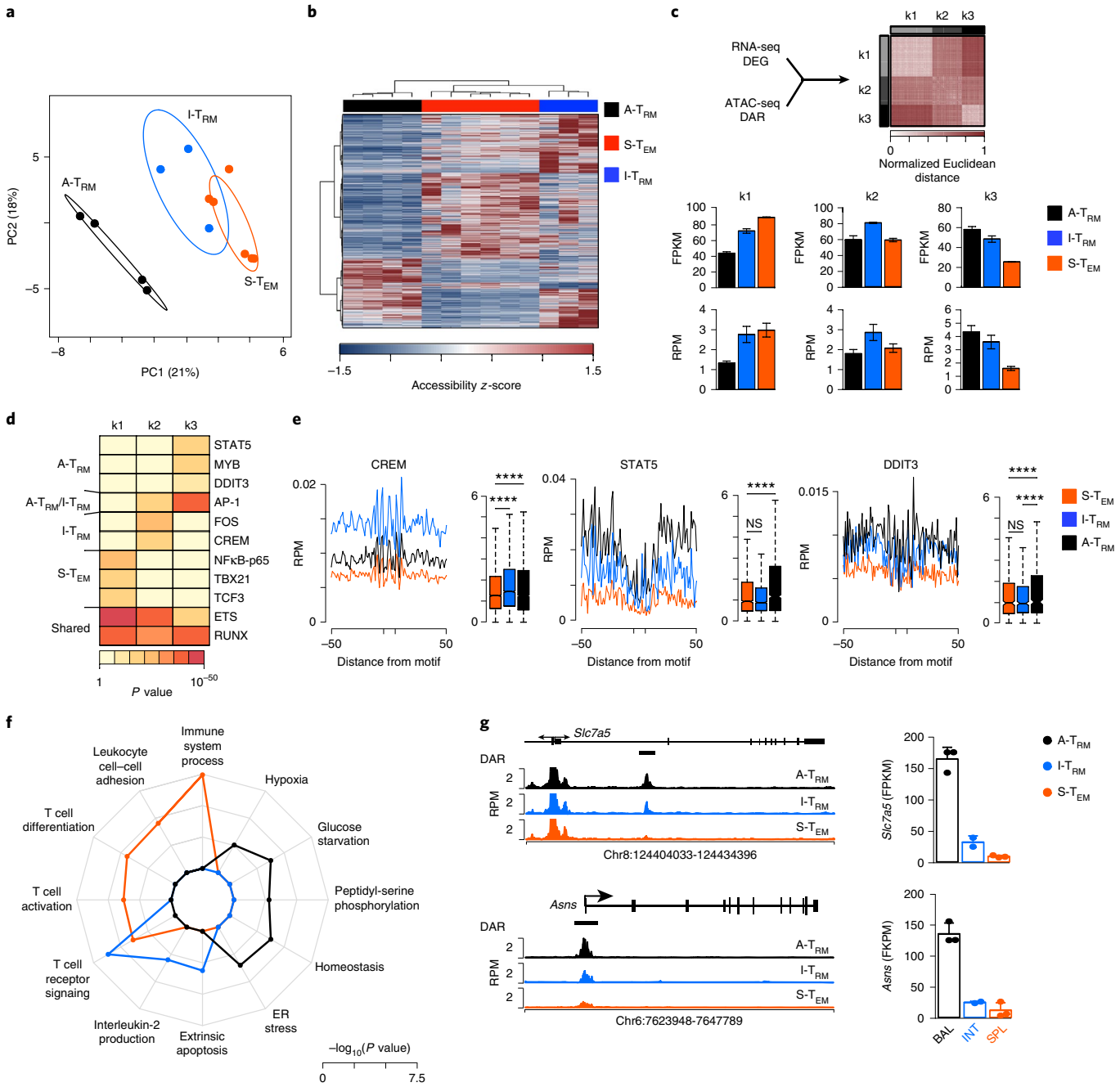

Fig. 4 | Chromatin accessibility reveals a distinct epigenetic programming of lung A-T$_{RM}$ and I-T$_{RM}$ populations. a, PCA of 47,683 accessible loci in A-T$_{RM}$, I-T$_{RM}$ or S-T$_{EM}$ cells from wild-type mice 35 d post-x31 infection. Circles represent 99% confidence intervals. BAL (A-T$_{RM}$, $n=4$), spleen (S-T$_{EM}$, $n=6$) and lung interstitium (I-T$_{RM}$, $n=3$). **b**, Heatmap of 8,772 DARs across A-T$_{RM}$, I-T$_{RM}$ or S-T$_{EM}$ cells as in **a**. **c**, Integrative analysis of DEGs from Fig. 3c and DARs from **b** using *k*-means clustering. Bar plots showing the expression (top) and accessibility (bottom) for A-T$_{RM}$, I-T$_{RM}$ or S-T$_{EM}$ cells in each of the k patterns. The data represent the mean ± s.d. **d**, Heatmap displaying the enrichment of transcription factor motifs for DARs within each of the k patterns from **c**. The *P* value was determined by HOMER using a binomial distribution. **e**, Histogram (left) and boxplot (right) of accessibility surrounding the indicated motif for A-T$_{RM}$, I-T$_{RM}$ or S-T$_{EM}$ cells. The boxplot center line indicates data median, lower and upper boundaries of boxes the 1st and 3rd quartile ranges, and whiskers the upper and lower ranges of the data. The data represent the mean accessibility for A-T$_{RM}$, I-T$_{RM}$ or S-T$_{EM}$ cells. The significance was determined using the two-tailed Student's *t*-test (*P* value: ****$P<0.0001$; NS, not significant). **f**, Radar plot of GO pathway enrichment for each of the k patterns from **c**. The significance was determined using Fisher's exact test. **g**, Genome plot (left) showing the accessibility pattern at the indicated loci for A-T$_{RM}$, I-T$_{RM}$ or S-T$_{EM}$ cells as in **a**. For each gene, the direction of transcription and the location of DARs are annotated. A barplot showing the expression of each gene is also depicted (right). The data represent the mean ± s.d. Chr, chromosome.

proapoptotic transcriptional regulation in response to stress (*Ddit3*) (Fig. 5a), suggesting that amino acid starvation could be the primary trigger for activation of the ISR in A-T$_{RM}$ cells[28]. GSEA indicated that gene sets involved in intrinsic apoptotic signaling, in response to ER stress and amino acid transport, were highly enriched in A-T$_{RM}$ cells compared with I-T$_{RM}$ and S-T$_{EM}$ cells (Fig. 5b), suggesting ISR activation and amino acid starvation in these cells. To further investigate the impact of the airway environment in the amino

acid stress response, we assessed the expression of the neutral amino acid transporter CD98, a heterodimer of Slc7a5 and Slc3a2 (ref. [29]), in combination with CD11a, which is highly expressed on memory CD8$^+$ T cells, but is downregulated within 36 h of entry into the airways[30], on FluNP$^+$ A-T_{RM}, I-T_{RM} and S-T_{EM} cells 35 d post-influenza infection. A-T_{RM} cells expressed more CD98 compared with I-T_{RM} and S-T_{EM} cells (Fig. 5c,d). Furthermore, increased expression of CD98 on A-T_{RM} cells was limited to CD11a^{lo} cells (Fig. 5d), indicating that upregulation of CD98 occurred after entry into the airway environment. To address whether the airway environment was sufficient to drive upregulation of CD98 on memory CD8$^+$ T cells, we transferred, intratracheally, S-T_{EM} cells, from wild-type mice infected with x31 30 d earlier, into naive, congenic, wild-type recipient mice. Expression of CD98 on transferred S-T_{EM} cells was notably increased 4 d post-intratracheal (i.t.) transfer compared with S-T_{EM} cells pre-transfer (Fig. 5e). In addition, expression of CD98 on S-T_{EM} cells transferred into the airways steadily increased between day 1 and day 8 post-i.t. transfer (Fig. 5f), suggesting that CD98 expression correlated with the length of time that memory CD8$^+$ T cells were in the airway environment.

To test whether amino acid starvation mediated the loss of A-T_{RM} cells under homeostatic conditions, we assessed whether deletion of *Ddit3*, a downstream regulator of apoptosis via amino acid starvation[31,32], which was upregulated in A-T_{RM} cells compared with I-T_{RM} and S-T_{EM} cells (Fig. 5g), increased the survival of A-T_{RM} cells. Chimeric mice generated by co-injecting wild-type and *Ddit3*$^{-/-}$ bone marrow cells into congenic mice were infected with influenza x31 8 weeks post-transfer. The number of FluNP$^+$ A-T_{RM}, I-T_{RM} and S-T_{EM} cells was determined at the peak of acute infection (day 10) and after establishment of T cell memory (day 60). The ratio of wild-type to *Ddit3*$^{-/-}$ FluNP$^+$ A-T_{RM} and I-T_{RM} cells (normalized to the ratio of wild-type to *Ddit3*$^{-/-}$ FluNP$^+$ S-T_{EM} cells in each mouse) showed no differences (Fig. 5h), indicating that *Ddit3* deficiency did not rescue the accumulation of FluNP$^+$ A-T_{RM} cells. However, the dynamic balance between cell death and cell recruitment that regulates the number of A-T_{RM} cells made it difficult to accurately define whether expression of *Ddit3* impacted the survival of memory CD8$^+$ T cells in the airway. Thus, to assess cell survival in the absence of cell recruitment to the airways, we sorted S-T_{EM} cells from the spleens of congenic wild-type CD45.1$^+$ and *Ddit3*$^{-/-}$ mice infected with x31 35 d earlier, and transferred them intratracheally in equal mixes into wild-type CD45.1$^+$CD45.2$^+$ recipients infected with x31 35 d earlier; 3 d post-transfer, the ratio of wild-type S-T_{EM} cells to *Ddit3*$^{-/-}$ S-T_{EM} cells in the airways was notably biased toward *Ddit3*$^{-/-}$ S-T_{EM} cells (Fig. 5i), indicating increased survival of *Ddit3*$^{-/-}$ S-T_{EM} cells in the airways compared with wild-type S-T_{EM} cells. To address whether deletion of *Ddit3* impacted cellular immunity, A-T_{RM} cells from wild-type or *Ddit3*$^{-/-}$ mice, infected with x31 35 d earlier, were transferred intratracheally into the airways of naive hosts before challenge with PR8 influenza 1 d post-transfer. Viral titers were similar between mice that received wild-type or *Ddit3*$^{-/-}$ A-T_{RM} cells on day 4 post-challenge (see Supplementary Fig. 5), indicating that expression of *Ddit3* did not alter the protective functions of A-T_{RM} cells. Thus, the airway environment affected T_{RM} cell biology and suggested that amino acid starvation contributed to the gradual loss of the A-T_{RM} cells.

The airway environment drives activation of the ISR. To provide a causative link between the microenvironment and the transcriptional signature of A-T_{RM} cells, we sorted FluNP$^+$ S-T_{EM} cells from wild-type (CD45.2) mice 35 d post-x31 infection, and transferred them intratracheally or intraperitoneally into wild-type CD45.1 mice that had been infected with x31 35 d earlier. RNA-seq on CD45.2$^+$ S-T_{EM} cells isolated from the airways or peritoneum on day 2 post-transfer found 375 transcripts altered in S-T_{EM} cells post-i.t. transfer compared with S-T_{EM} cells pre-transfer, whereas only 54 transcripts were differentially expressed in S-T_{EM} cells post-intraperitoneal (i.p.) transfer compared with S-T_{EM} cells pre-transfer (Fig. 6a). GSEA comparing S-T_{EM} cells post-i.t. or post-i.p. transfer with S-T_{EM} cells pre-transfer indicated an important enrichment for pathways mediating the amino acid starvation response and ER stress in post-i.t. transfer S-T_{EM} cells, but not post-i.p. transfer S-T_{EM} cells (Fig. 6b)[33]. Published datasets from alveolar and lung interstitial macrophages showed no enrichment of genes involved in amino acid starvation or ER stress (see Supplementary Fig. 6), indicating that these pathways were enriched in S-T_{EM} cells but not in macrophages exposed to the airway environment.

Cellular stress due to nutrient-poor conditions in the airway may limit the lifespan and effector functions of airway T_{RM} cells during homeostasis to prevent unnecessary immunopathology. To assess whether an inflamed airway environment had a similar impact on the programming of T_{EM} cells, FluNP$^+$ S-T_{EM} cells isolated from CD45.2 wild-type mice 35 d post-x31 infection were transferred intratracheally into the airways of CD45.1 wild-type mice 8 d post-infection with Sendai virus (post-i.t. acute) or 35 d post-infection with Sendai virus (post-i.t. memory), based on the fact that influenza and Sendai viruses are antigenically distinct and share no cross-reactive T cell epitopes[4]. Comparison of RNA-seq on CD45.2$^+$ S-T_{EM} cells, isolated on day 2 post-i.t. transfer from post-i.t. acute mice or post-i.t. memory mice, found over 400 DEGs (Fig. 6c). Genes related to amino acid starvation (*Sars*, *Slc7a5*) and those related to cell survival (*Myc*, *Bbc3*) were notably increased in post-i.t. memory S-T_{EM} cells compared with post-i.t. acute S-T_{EM} cells (Fig. 6c). Analysis of gene expression from pre-transfer, post-i.t. memory, post-i.t. acute and post-i.p. S-T_{EM} cells showed similar expression of *Sars* and *Slc7a5* in pre-transfer, post-i.p. and post-i.t. acute S-T_{EM} cells (Fig. 6d), indicating that the amino acid starvation response was not induced in S-T_{EM} cells transferred into acutely infected airways. Expression of the amino acid transporter CD98 was higher on post-i.t. memory S-T_{EM} cells compared with post-i.p. and post-i.t. acute S-T_{EM} cells (Fig. 6e), confirming the RNA-seq results. Thus, the airway microenvironment could drive activation of the amino acid stress response pathway in S-T_{EM} cells at steady state, but did not do so during infection.

The airway environment regulates the A-T_{RM} cell genetic program. To determine the gene signatures induced by the airway environment alone, compared with those induced during the differentiation of A-T_{RM} cells after viral clearance, we compared the genes differentially expressed in A-T_{RM} cells versus S-T_{EM} cells, isolated from wild-type mice 35 d post-x31 infection, with genes differentially expressed in S-T_{EM} cells pre-transfer and post-i.t. transfer. A number of genes associated with amino acid starvation, such as *Slc7a5*, *Asns* and *Myc*, were upregulated in both A-T_{RM} cells and post-i.t. transfer S-T_{EM} cells, whereas known T_{RM} genes such as *Itgae* and *Itga1* were upregulated only in A-T_{RM} cells, but not post-i.t. transfer S-T_{EM} cells, and independent of the tissue environment (Fig. 7a). Comparisons of select DEGs across A-T_{RM}, I-T_{RM}, S-T_{EM}, and pre- and post-i.t. transfer S-T_{EM} cells indicated that, although DEGs associated with cell stress (*Aars* and *Slc7a5*) or lack of CTL activity (*Gzmb*) were observed only in A-T_{RM} cells and post-i.t. transfer S-T_{EM} cells exposed to the airway environment, known T_{RM} genes (*Itgae*, *Itga1* and *Cxcr6*) were similarly differentially expressed in A-T_{RM} cells and I-T_{RM} cells compared with S-T_{EM} cells and pre- and post-i.t. transfer S-T_{EM} cells (Fig. 7b). These data indicated that the program linked to lung T_{RM} cell differentiation was shared between A-T_{RM} and I-T_{RM} cells, with subsequent differences in gene expression being driven by adaptations to the local environment.

As activation of the ISR was a key adaptation of A-T_{RM} cells to their environment, we examined the impact of nutrient restoration on A-T_{RM} cells. After 2 d of in vitro culture without any stimulation, A-T_{RM} cells from wild-type mice infected with x31 35 d earlier

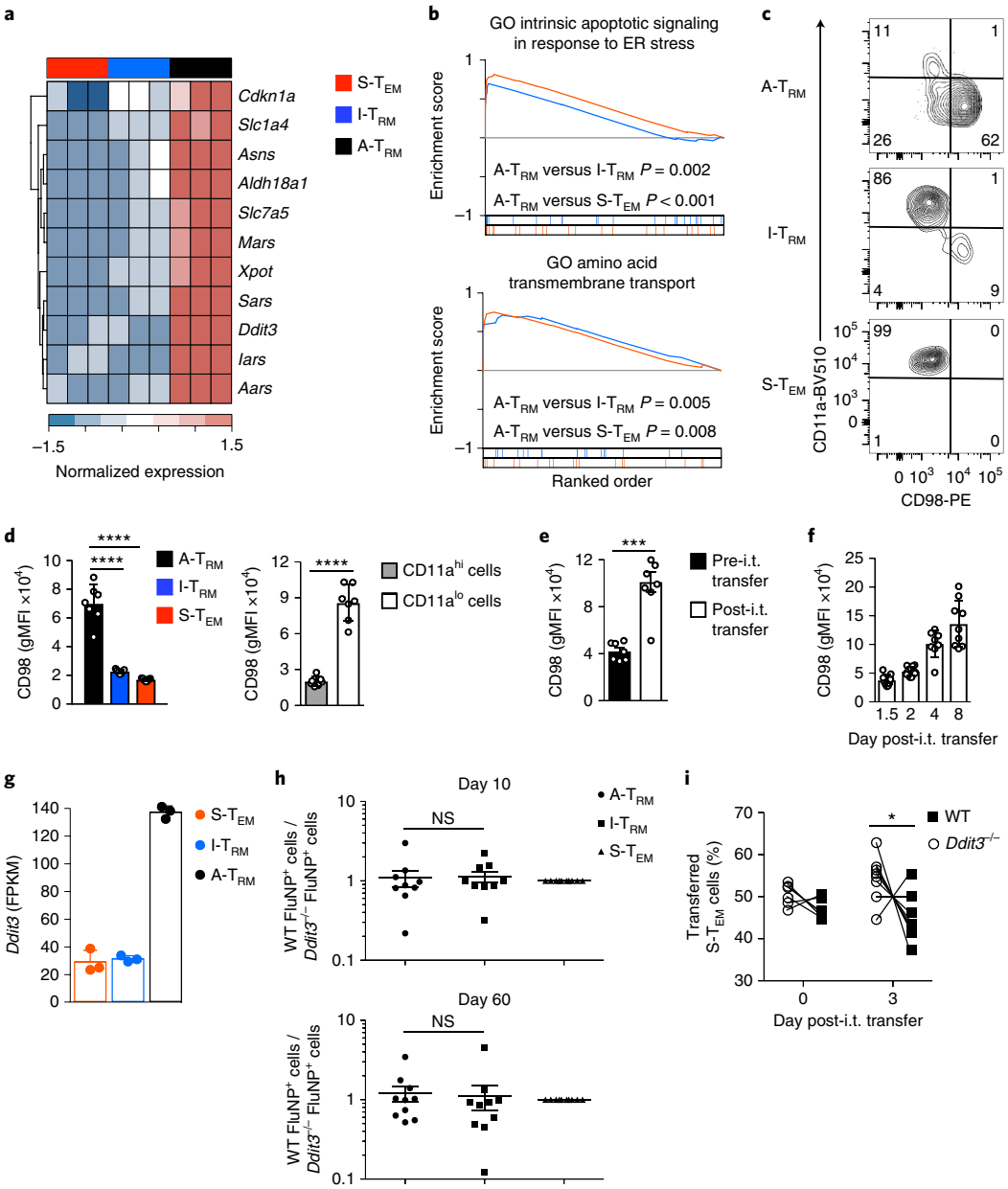

Fig. 5 | Exposure to the airway environment drives activation of the ISR. a, Heatmap for selected ISR genes associated with the amino acid starvation response in A-T_{RM}, I-T_{RM} or S-T_{EM} cells from wild-type mice 35 d post-x31 infection. **b**, GSEA of intrinsic apoptotic signaling in response to ER stress and amino acid transmembrane transport gene sets, comparing A-T_{RM} cells with I-T_{RM} cells and A-T_{RM} cells with S-T_{EM} cells as in **a**. **c**, CD11a and CD98 staining on FluNP⁺ A-T_{RM}, I-T_{RM} and S-T_{EM} cells from wild-type mice 35 d post-x31 infection. **d**, Geometric mean fluorescence intensity (gMFI) of CD98 measured on FluNP⁺CD69⁺ A-T_{RM}, I-T_{RM}, and S-T_{EM} cells, and on FluNP⁺CD11a^{hi} or FluNP⁺CD11a^{lo} A-T_{RM} cells, from wild-type mice 35 d after x31 infection ($n = 7$, representing two experiments). The significance was determined using the two-tailed Student's *t*-test. **e**, The gMFI of CD98 on S-T_{EM} cells isolated from wild-type mice 35 d post-x31 infection, either pre-transfer or 4 d post-i.t. transfer ($n = 8$, combined from two experiments). The significance was determined using the Mann–Whitney *U*-test. **f**, The gMFI of CD98 on S-T_{EM} cells as in **e** from days 1–8 post-i.t. transfer ($n = 8$–12, combined from two experiments). **g**, Expression of *Ddit3* by RNA-seq in A-T_{RM}, I-T_{RM} and S-T_{EM} cells as in **a**, shown as FPKM. The data represent the mean ± s.d. **h**, The ratio of wild-type (WT) to *Ddit3*$^{-/-}$ FluNP⁺ A-T_{RM} and I-T_{RM} cells normalized to the ratio of FluNP⁺ S-T_{EM} cells from mixed bone marrow chimeras infected with x31 on day 10 or day 60 post-infection ($n = 9$ mice at day 10, 10 mice at day 60, representing two experiments). **i**, Frequency of CD45.1⁺ wild-type and *Ddit3*$^{-/-}$ S-T_{EM} cells sorted from the spleen on day 35 post-x31 infection before (day 0) or 3 d after i.t. transfer into CD45.1⁺CD45.2⁺ recipient mice. The data are represented as mean ± s.d. The significance was determined using the paired Student's *t*-test. *P* values are as follows: $^{*}P < 0.05$, $^{**}P < 0.01$, $^{***}P < 0.001$, $^{****}P < 0.0001$.

showed 1,698 DEGs (FDR < 0.05, absolute $\log_2$(FC) > 1) compared with A-T_{RM} cells before in vitro culture, whereas S-T_{EM} cells cultured in vitro showed only 9 DEGs compared with S-T_{EM} cells before in vitro culture (Fig. 7c). DEGs from in vitro A-T_{RM} cells were grouped in three clusters, and GO analyses indicated processes involved in apoptosis, tRNA charging and responses to ER stress being notably altered in A-T_{RM} cells after in vitro culture (Fig. 7d). Genes related to the ISR (*Slc7a5*, *Slc3a2*, *Ddit3*, *Sars*, *Aars* and *Bbc3*)[34] were downregulated in A-T_{RM} cells cultured in a nutrient-rich environment compared with A-T_{RM} cells isolated directly

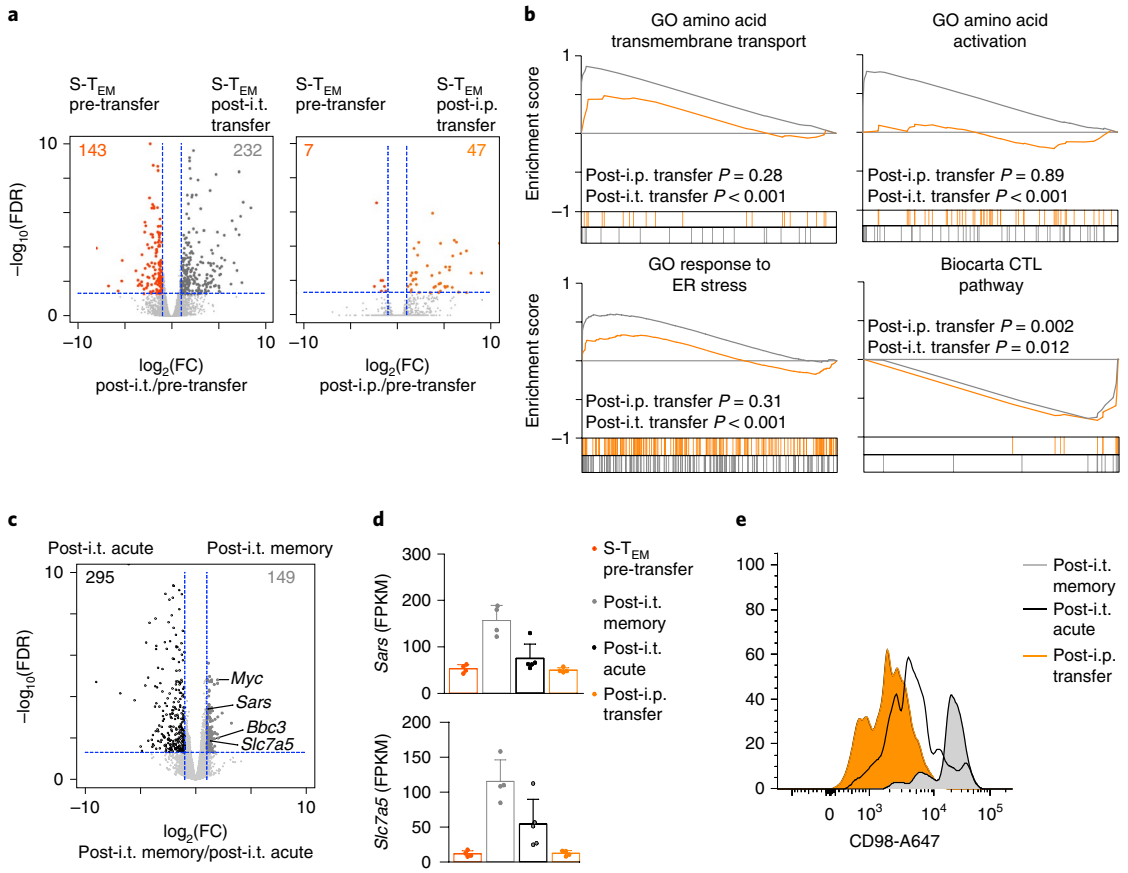

Fig. 6 | The airway environment is sufficient to alter the transcriptional program of S-T_{EM} cells but does not induce core T_{RM} programming. a, Volcano plots of DEGs between pre-transfer S-T_{EM} ($n = 4$) and post-i.t. transfer S-T_{EM} ($n = 4$) or post-i.p. transfer S-T_{EM} ($n = 4$) cells, sorted from the spleen of CD45.2$^+$ wild-type mice on day 35 post-x31 infection and transferred into congenic CD45.1$^+$ mice that had been infected with x31 35 d earlier. Transferred CD45.2$^+$ cells were isolated 2 d post-transfer for RNA-seq analysis. Example genes are highlighted and the number of DEGs are indicated. **b**, GSEA on post-i.t. transfer S-T_{EM} and post-i.p. transfer S-T_{EM} cells as in **a** using the indicated gene sets. **c**, Volcano plot of DEGs comparing post-i.t. transfer S-T_{EM} cells sorted from the spleen of CD45.2$^+$ wild-type mice on day 35 post-x31 infection, and transferred into the airways of congenic CD45.1$^+$ mice that were infected with Sendai virus 8 d (post-i.t. acute) or 35 d (post-i.t. memory) earlier. Transferred CD45.2$^+$ cells were isolated 2 d post-transfer for RNA-seq analysis. Example genes are highlighted and the number of DEGs are indicated ($n = 5$ for acute transfer samples, $n = 4$ for memory transfer samples). **d**, Barplot showing the expression of cell stress genes (*Sars*, *Slc7a5*) in pre-transfer S-T_{EM}, post-i.t. memory S-T_{EM}, post-i.t. acute S-T_{EM} and post-i.p. memory S-T_{EM} cells, as in **a** and **c**. The data represent the mean ± s.d. **e**, CD98 staining on post-i.t. memory S-T_{EM}, post-i.t. acute S-T_{EM} and post-i.p. memory S-T_{EM} cells as in **a** and **c**.

from the airways (Fig. 7f,g), indicating that this pathway was reversible and driven by the local microenvironment. These observations defined the key transcriptional programs induced by the differentiation of T_{RM} cells versus the airway environment, and showed that the ISR driven by amino acid starvation could be rescued by nutrients in the local microenvironment.

Discussion

In the present study, we found that A-T_{RM} and I-T_{RM} cells have different transcriptional and epigenetic profiles due to their unique localization within the tissue. A-T_{RM} cells showed increased apoptosis, decreased expression of cytolytic genes and a transcriptional signature indicative of increased cellular stress due to amino acid starvation. Comparisons of naturally generated A-T_{RM} cells and S-T_{EM} cells transferred into the airways indicated that expression of core T_{RM} genes was largely unaffected by the environment, and was instead regulated during initial T_{RM} cell differentiation after viral clearance. Thus, the lung CD8$^+$ T_{RM} pool comprised functionally and genetically distinct A-T_{RM} and I-T_{RM} cell populations that shared a common T_{RM} cell differentiation program, but were further shaped by their respective microenvironments.

The CD8$^+$ T_{RM} cell core lineage programming shared by both A-T_{RM} and I-T_{RM} cells is driven by interactions between the transcription factors Blimp1 and Hobit[6]. However, A-T_{RM} cells were also enriched in *Ddit3* motifs and coordinately upregulated genes in the amino acid starvation response, with distinct accessible chromatin peaks at stress response genes such as *Slc7a5* and *Asns*. Consistent with the concept that T_{RM} cell molecular programming is both lineage and environmentally determined[22,23], we observed only a partial adoption of the A-T_{RM} cell program after i.t. transfer of S-T_{EM} cells into the airways. The amino acid stress response, but not core T_{RM} genes, was induced after i.t. transfer, indicating that the core transcriptional program of A-T_{RM} cells was not driven by exposure to the local microenvironment. Thus, these data identify a common lung T_{RM} signature, distinct from the impact of different microenvironments within the lung.

A-T_{RM} cells are known to have a limited lifespan[30,35]. The waning of the A-T_{RM} cell pool over time had suggested that the source of these newly recruited cells must also be similarly transient, but whether these cells come predominantly from the circulation or from within the tissue remained unclear. Our parabiosis experiments in mice previously exposed to influenza virus indicated that

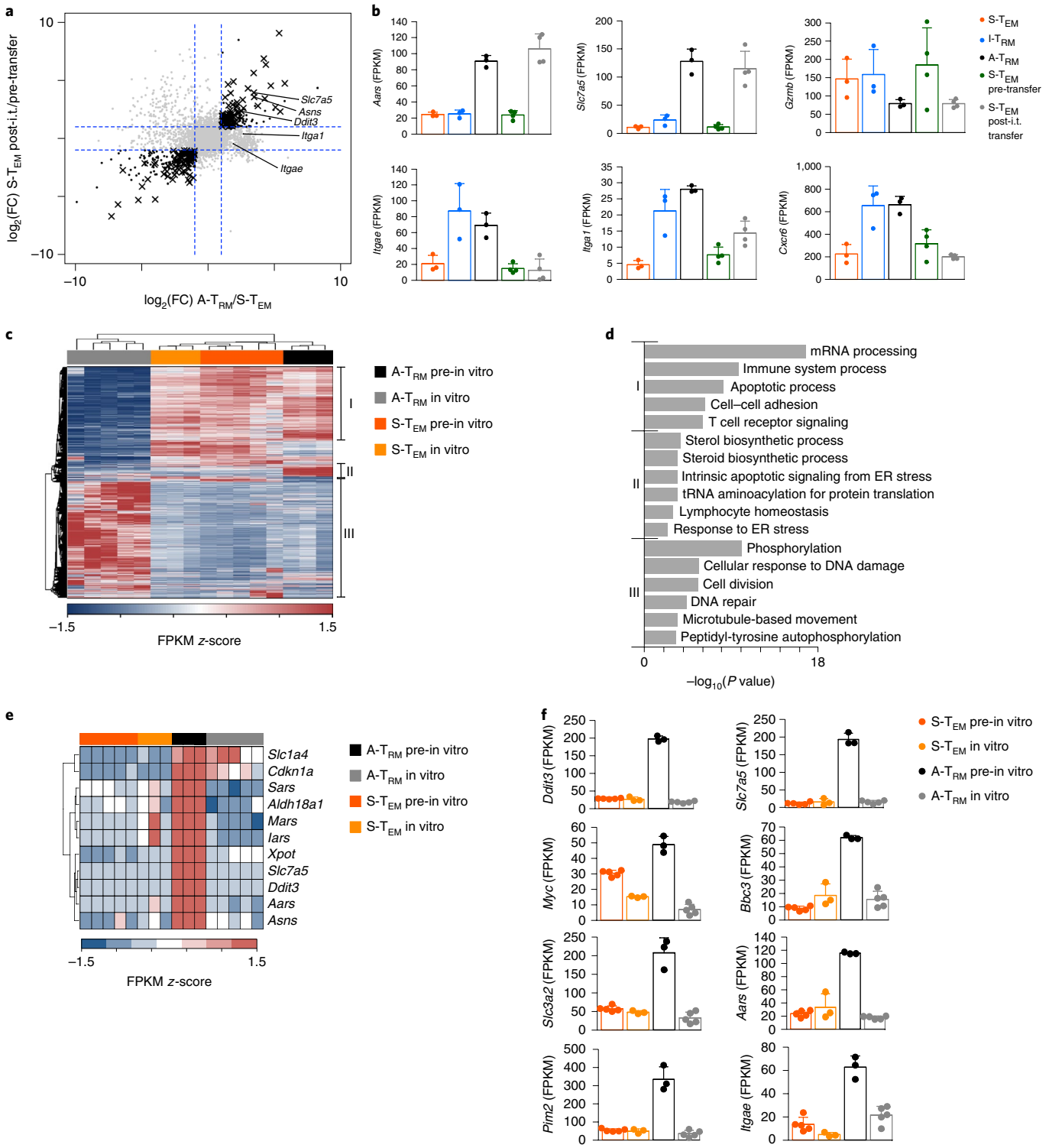

Fig. 7 | Restoration of a nutrient-rich environment resolves environmentally driven cellular stress in A-T_{RM} cells. a, Scatterplot correlating the DEGs between pre-transfer S-T_{EM} cells and post-i.t. memory S-T_{EM} cells as in Fig. 6a versus DEGs between A-T_{RM} and S-T_{EM} cells as in Fig. 3a. The location of select genes is indicated. X indicates DEGs in both comparisons. **b**, Barplot showing the expression of cell stress (*Aars*, *Slc7a5*) and T_{RM} (*Itgae*, *Itga1*, *Gzmb* and *Cxcr6*) signature genes from A-T_{RM}, I-T_{RM}, S-T_{EM}, pre-transfer S-T_{EM} and post-i.t. transfer S-T_{EM} cells. The data represent the mean ± s.d. **c**, Heatmap of 5,715 DEGs comparing S-T_{EM} and A-T_{RM} cells sorted from wild-type mice 35 d post-x31 infection before (pre-in vitro) and 2 d after (post-in vitro) culture ($n = 5$ for A-T_{RM} cells, $n = 3$ for S-T_{EM} cells). **d**, GO pathway analysis for three distinct regions of gene expression from A-T_{RM} pre-in vitro, A-T_{RM} post-in vitro, S-T_{EM} pre-in vitro and S-T_{EM} in vitro cells as in **c**. The significance was determined using Fisher's exact test. **e**, Heatmap for selected ISR genes associated with the amino acid starvation response from A-T_{RM} pre-in vitro, A-T_{RM} post-in vitro, S-T_{EM} pre-in vitro and S-T_{EM} in vitro cells as in **c**. **f**, Barplot showing the expression of amino acid stress (*Slc7a5*, *Slc3a2*, *Aars*), proapoptotic (*Ddit3*, *Bbc3*), cell stress (*Myc*, *Pim2*) and cell adhesion (*Itgae*) genes in A-T_{RM} pre-in vitro, A-T_{RM} post-in vitro, S-T_{EM} pre-in vitro and S-T_{EM} in vitro cells as in **c**. The data represent the mean ± s.d.

A-T_{RM} and I-T_{RM} cells were not maintained by recruitment of circulating cells into the lung T_{RM} cell pool, which agrees with recent reports that antigen encounter in the pulmonary environment, and not simply entry into the lung tissue itself, is required for T_{RM} cell differentiation[14,36,37]. These data are in contrast to a study showing that circulating T_{EM} cells were able to re-seed the lung T_{RM} cell pool[16]. The observation that lung T_{RM} cells could develop independently of pulmonary antigen encounter under specific inflammatory conditions may explain this discrepancy[38]. Thus, there may be scenarios where circulating T_{EM} cells can convert into lung T_{RM} cells, but further investigation is required to define these antigen-independent mechanisms.

Results in animal models of respiratory viral infections indicate that the poor longevity of A-T_{RM} and I-T_{RM} cells would be an impediment to the development of cell-mediated vaccines. However, approaches to maintain lung T_{RM} cells and protective cellular immunity for at least 1 year have been reported[39,40]. Comparison of primary and quaternary $CD8^+$ T cell memory indicates that lung T_{RM} cells generated by repeated influenza infections are resistant to apoptosis and persist in larger numbers[39], suggesting that prime-boost strategies may improve lung T_{RM} cell survival. In addition, vaccination with replication-defective adenoviruses expressing 4-1BBL sustained lung T_{RM} cells and prolonged heterosubtype immunity[40]. Additional research into the mechanisms behind the longevity of lung T_{RM} cells is needed to inform the design of efficacious cell-mediated vaccine strategies.

The advantage or utility of relatively short-lived A-T_{RM} cells remains unclear. Severe influenza infections are accompanied by extensive tissue damage that leads to fluid leakage in the airspaces. Under these conditions, the airways could become an environment rich in nutrients and amino acids, and virus-specific $CD8^+$ T cells would thus be able to maintain their cytolytic function and promote viral clearance[41]. In contrast, the nutrient-poor conditions in the airway during homeostasis may serve as a brake on CTL activity to avoid unnecessary damage to the epithelium. Notably, this nutrient-poor environment does not influence the secretion of antiviral cytokines such as interferon-γ, which is critical for the protection mediated by A-T_{RM} cells[15]. Therefore, the difference in nutrient availability among distinct microenvironments of the lung may create a division of labor among the lung T_{RM} cell pool, with A-T_{RM} cells serving primarily a 'sensing and alarm' function that could recruit cytolytic I-T_{RM} cells and other immune cells to the site of infection[2].

In summary, our results indicate that the lung T_{RM} cell pool comprised two distinct subsets—A-T_{RM} cells and I-T_{RM} cells—with distinct functions shaped by epigenetic reprogramming in response to environmental cues. Developing a more thorough understanding of how tissue microenvironments in the lung influence the genetic program of T_{RM} cells, and defining mechanisms by which cells adapt to and possibly overcome these challenging environments, will assist in the rational design of cell-mediated vaccines against respiratory pathogens.

Online content

Any methods, additional references, Nature Research reporting summaries, source data, extended data, supplementary information, acknowledgements, peer review information; details of author contributions and competing interests; and statements of data and code availability are available at https://doi.org/10.1038/s41590-019-0584-x.

Received: 16 November 2018; Accepted: 16 December 2019;
Published online: 17 January 2020

References

1. Gebhardt, T. et al. Memory T cells in nonlymphoid tissue that provide enhanced local immunity during infection with herpes simplex virus. *Nat. Immunol.* **10**, 524–530 (2009).
2. Schenkel, J. M., Fraser, K. A., Vezys, V. & Masopust, D. Sensing and alarm function of resident memory $CD8^+$ T cells. *Nat. Immunol.* **14**, 509–513 (2013).
3. Jiang, X. et al. Skin infection generates non-migratory memory $CD8^+$ T_{RM} cells providing global skin immunity. *Nature* **483**, 227–231 (2012).
4. Kohlmeier, J. E., Cookenham, T., Roberts, A. D., Miller, S. C. & Woodland, D. L. Type I interferons regulate cytolytic activity of memory $CD8^+$ T cells in the lung airways during respiratory virus challenge. *Immunity* **33**, 96–105 (2010).
5. Mackay, L. K. et al. T-box transcription factors combine with the cytokines TGF-β and IL-15 to control tissue-resident memory T cell fate. *Immunity* **43**, 1101–1111 (2015).
6. Mackay, L. K. et al. Hobit and Blimp1 instruct a universal transcriptional program of tissue residency in lymphocytes. *Science* **352**, 459–463 (2016).
7. Liang, S. H., Mozdzanowska, K., Palladino, G. & Gerhard, W. Heterosubtypic immunity to influenza type-A virus in mice—effector mechanisms and their longevity. *J. Immunol.* **152**, 1653–1661 (1994).
8. Wu, T. et al. Lung-resident memory CD8 T cells (T_{RM}) are indispensable for optimal cross-protection against pulmonary virus infection. *J. Leukoc. Biol.* **95**, 215–224 (2014).
9. Purwar, R. et al. Resident memory T cells (T_{RM}) are abundant in human lung: diversity, function, and antigen specificity. *PLoS One* **6**, e16245 (2011).
10. Lee, L. Y. et al. Memory T cells established by seasonal human influenza A infection cross-react with avian influenza A (H5N1) in healthy individuals. *J. Clin. Invest.* **118**, 3478–3490 (2008).
11. Hogan, R. J. et al. Activated antigen-specific $CD8^+$ T cells persist in the lungs following recovery from respiratory virus infections. *J. Immunol.* **166**, 1813–1822 (2001).
12. Hou, S., Doherty, P. C., Zijlstra, M., Jaenisch, R. & Katz, J. M. Delayed clearance of Sendai virus in mice lacking class I MHC-restricted $CD8^+$ T cells. *J. Immunol.* **149**, 1319–1325 (1992).
13. Eichelberger, M., Allan, W., Zijlstra, M., Jaenisch, R. & Doherty, P. C. Clearance of influenza virus respiratory infection in mice lacking class I major histocompatibility complex-restricted $CD8^+$ T cells. *J. Exp. Med.* **174**, 875–880 (1991).
14. McMaster, S. R. et al. Pulmonary antigen encounter regulates the establishment of tissue-resident CD8 memory T cells in the lung airways and parenchyma. *Mucosal Immunol.* **11**, 1071–1078 (2018).
15. McMaster, S. R., Wilson, J. J., Wang, H. & Kohlmeier, J. E. Airway-resident memory CD8 T cells provide antigen-specific protection against respiratory virus challenge through rapid IFN-γ production. *J. Immunol.* **195**, 203–209 (2015).
16. Slutter, B. et al. Dynamics of influenza-induced lung-resident memory T cells underlie waning heterosubtypic immunity. *Sci. Immunol.* **2**, eaag2031 (2017).
17. Farber, D. L., Yudanin, N. A. & Restifo, N. P. Human memory T cells: generation, compartmentalization and homeostasis. *Nat. Rev. Immunol.* **14**, 24–35 (2014).
18. Kumar, B. V. et al. Human tissue-resident memory T cells are defined by core transcriptional and functional signatures in lymphoid and mucosal sites. *Cell Rep.* **20**, 2921–2934 (2017).
19. Hombrink, P. et al. Programs for the persistence, vigilance and control of human $CD8^+$ lung-resident memory T cells. *Nat. Immunol.* **17**, 1467–1478 (2016).
20. Hikono, H. et al. Activation phenotype, rather than central- or effector-memory phenotype, predicts the recall efficacy of memory $CD8^+$ T cells. *J. Exp. Med.* **204**, 1625–1636 (2007).
21. Subramanian, A. et al. Gene set enrichment analysis: a knowledge-based approach for interpreting genome-wide expression profiles. *Proc. Natl Acad. Sci. USA* **102**, 15545–15550 (2005).
22. Gosselin, D. et al. Environment drives selection and function of enhancers controlling tissue-specific macrophage identities. *Cell* **159**, 1327–1340 (2014).
23. Lavin, Y. et al. Tissue-resident macrophage enhancer landscapes are shaped by the local microenvironment. *Cell* **159**, 1312–1326 (2014).
24. Buenrostro, J. D., Giresi, P. G., Zaba, L. C., Chang, H. Y. & Greenleaf, W. J. Transposition of native chromatin for fast and sensitive epigenomic profiling of open chromatin, DNA-binding proteins and nucleosome position. *Nat. Methods* **10**, 1213–1218 (2013).
25. Scharer, C. D. et al. ATAC-seq on biobanked specimens defines a unique chromatin accessibility structure in naive SLE B cells. *Sci. Rep.* **6**, 27030 (2016).
26. Barwick, B. G., Scharer, C. D., Bally, A. P. & Boss, J. M. Plasma cell differentiation is coupled to division-dependent DNA hypomethylation and gene regulation. *Nat. Immunol.* **17**, 1216–1225 (2016).
27. Scharer, C. D., Bally, A. P., Gandham, B. & Boss, J. M. Cutting edge: chromatin accessibility programs CD8 T cell memory. *J. Immunol.* **198**, 2238–2243 (2017).
28. Pakos-Zebrucka, K. et al. The integrated stress response. *EMBO Rep.* **17**, 1374–1395 (2016).
29. de la Ballina, L. R. et al. Amino acid transport associated to cluster of differentiation 98 heavy chain (CD98hc) is at the cross-road of oxidative stress and amino acid availability. *J. Biol. Chem.* **291**, 9700–9711 (2016).

30. Ely, K. H., Cookenham, T., Roberts, A. D. & Woodland, D. L. Memory T cell populations in the lung airways are maintained by continual recruitment. *J. Immunol.* **176**, 537–543 (2006).
31. Li, T. et al. DDIT3 and KAT2A proteins regulate TNFRSF10A and TNFRSF10B expression in endoplasmic reticulum stress-mediated apoptosis in human lung cancer cells. *J. Biol. Chem.* **290**, 11108–11118 (2015).
32. Pino, S. C. et al. CHOP mediates endoplasmic reticulum stress-induced apoptosis in Gimap5-deficient T cells. *PLoS One* **4**, e5468 (2009).
33. Teske, B. F. et al. CHOP induces activating transcription factor 5 (ATF5) to trigger apoptosis in response to perturbations in protein homeostasis. *Mol. Biol. Cell* **24**, 2477–2490 (2013).
34. Iyer, V. R. et al. The transcriptional program in the response of human fibroblasts to serum. *Science* **283**, 83–87 (1999).
35. Kohlmeier, J. E., Miller, S. C. & Woodland, D. L. Cutting edge: antigen is not required for the activation and maintenance of virus-specific memory CD8$^+$ T cells in the lung airways. *J. Immunol.* **178**, 4721–4725 (2007).
36. Takamura, S. et al. Specific niches for lung-resident memory CD8$^+$ T cells at the site of tissue regeneration enable CD69-independent maintenance. *J. Exp. Med.* **213**, 3057–3073 (2016).
37. Pizzolla, A. et al. Resident memory CD8$^+$ T cells in the upper respiratory tract prevent pulmonary influenza virus infection. *Sci. Immunol.* **2**, eaam6970 (2017).
38. Caminschi, I., Lahoud, M. H., Pizzolla, A. & Wakim, L. M. Zymosan by-passes the requirement for pulmonary antigen encounter in lung tissue-resident memory CD8$^+$ T cell development. *Mucosal Immunol.* **12**, 403–412 (2019).
39. Van Braeckel-Budimir, N., Varga, S. M., Badovinac, V. P. & Harty, J. T. Repeated antigen exposure extends the durability of influenza-specific lung-resident memory CD8$^+$ T cells and heterosubtypic immunity. *Cell Rep.* **24**, 3374–3382.e3 (2018).
40. Zhou, A. C., Wagar, L. E., Wortzman, M. E. & Watts, T. H. Intrinsic 4-1BB signals are indispensable for the establishment of an influenza-specific tissue-resident memory CD8 T-cell population in the lung. *Mucosal Immunol.* **10**, 1294–1309 (2017).
41. Mintern, J. D., Guillonneau, C., Carbone, F. R., Doherty, P. C. & Turner, S. J. Cutting edge: tissue-resident memory CTL down-regulate cytolytic molecule expression following virus clearance. *J. Immunol.* **179**, 7220–7224 (2007).

Methods

Mice. C57BL/6J (WT), B6.SJL-Ptprca Pepc^{b}/BoyJ (CD45.1) and B6.129S(Cg)-*Ddit3*$^{tm2.1Dron}$/J (*Ddit3*$^{-/-}$) mice were purchased from the Jackson Laboratory and colonies were maintained at Emory University in specific pathogen-free conditions. Mice were aged between 8 and 13 weeks at the time of infection and housed under specific animal biosafety level 2 conditions after infection. All experiments were completed in accordance with the Institutional Animal Care and Use Committee (IACUC) guidelines of Emory University and Kindai University.

Infections. Mice were anesthetized with 300 mg kg^{-1} of either Avertin (2,2,2-tribromoethanol, Sigma) or isoflurane (Patterson Veterinary) before infection. Mice were infected intranasally with 30,000 EID_{50} (50% egg infectious doses) influenza A/HKx31 (x31, H3N2) or 3,000 EID_{50} Sendai virus in a total volume of 30 µl. Heterologous challenge of x31-immune mice was performed with a dose of 10 LD_{50} (median lethal dose; 3,000 plaque-forming units) of influenza A/PR8 (PR8, H1N1) in 50 µl. Challenged mice were monitored daily for weight loss and humanely euthanized if they fell below 75% of their original weight in accordance with Emory IACUC guidelines.

Intravenous labeling, single cell isolation and staining. Mice were intravenously labeled via tail vein injection under a heat lamp with either CD3e (1.5 µg of fluorophore-conjugated α-CD3ε antibody in 200 µl of phosphate-buffered saline (PBS)) or CD45.2 (2 µg of fluorophore-conjugated α-CD45.2 antibody in 200 µl of PBS). Mice were euthanized, 5 min after an intravenous injection, with Avertin. and exsanguinated before harvest of BAL, lung and other tissues. Lung and other tissues were disassociated as previously described[15]. Single cell isolations were Fc blocked using the antibody 2.4G2. Then they were surface stained with tetramers at room temperature for 1 h, followed by surface staining with listed antibodies. Cell viability was determined using either Zombie NIR (BioLegend) or 7AAD. Tetramers were against influenza epitopes $NP_{366-374}$ D^{b} and $PA_{224-233}$ D^{b}. For in vitro cultures, total BAL and CD8^{+} T cell-enriched spleens from influenza-immune mice were plated in round-bottomed plates in R10 (RPMI, 10% fetal bovine saline and 1% penicillin, streptomycin and glutamine) for 48 h in a 5% CO_2 incubator at 37 °C before sorting for RNA isolation and downstream analysis. For RNA-seq samples, CD8^{+}CD44^{Hi}, CD62L^{-} T cells were sorted from the BAL and spleen pre- and post-in vitro culture.

Antibodies and flow cytometry.

Marker	Clone	Manufacturer
CD8	53-6.7	BioLegend
CD4	RM-45	BioLegend
CD69	H1.2F3	BioLegend
CD103	M290	BD
CD103	2E7	BioLegend
CD11a	M17I4	BD
CD11a	M17I4	Invitrogen
CD44	IM7	Ebioscience
CD44	IM7	BioLegend
CD62L	MEL-14	BioLegend
Zombie NIR	-	BioLegend
7AAD	-	BioLegend
CD3e	145-2C11	BD
CD45.2	104	BioLegend
CD98	RL388	BioLegend
CXCR3	CXCR3-173	BioLegend
CD45.1	A20	BioLegend
Annexin V	-	BioLegend
BCL2	3F11	BD

Tetramers were provided by the National Institutes of Health (NIH) Tetramer Core Facility at Emory (H-2D^{b} Influenza A NP 366-374 (ASNENMETM) and H-2D^{b} Influenza A PA 224–233 (SSLENFRAYV)). All samples were run on an LSRII or Fortessa X20 (BD Biosciences) flow cytometer, or sorted on a FACSAria II (BD Biosciences). Flow cytometry data were analyzed using FlowJo v.10 software.

Parabiotic surgery. Parabiotic surgery was performed as described[36] with the following modification: each parabiont partner was infected with x31 (30,000 EID_{50}) and allowed to mature to a memory time point (28 d), then stitched together and maintained as parabiont pairs for 3 weeks. Equilibration was confirmed in the peripheral blood before separation, intravital labeling and analysis.

Mixed bone marrow chimeras. Mixed bone marrow chimeras were generated as previously described[42] and allowed to reconstitute for 8 weeks before infection. CD45.1 and *Ddit3*$^{-/-}$ mice were used as bone marrow donors, and CD45.2/CD45.1 heterozygous mice were used as recipients. Mice were irradiated using an RS2000 X-ray irradiator (Rad Source) and received 2 doses of 4.75 Gy, 6 h apart.

Intratracheal and intraperitoneal transfers. Intratracheal and intraperitoneal transfers were performed as described[15,35]. Cells were isolated from the spleens of x31-immune mice (35–100 d post-infection) and sorted on the CD8^{+}CD44^{Hi}, CD62L^{-} population to isolate T_{EM} cells. Between 5×10^{4} and 10×10^{4} cells were transferred intratracheally or intraperitoneally into congenic, infection-matched recipient mice and cells were collected by BAL or peritoneal lavage 2 d later. Cells were sorted on the basis of congenic marker staining to isolate transferred cells for downstream analysis.

Viral titers. Lung viral titers were measured after PR8 infection of naive congenic mice receiving either wild-type- or *Ddit3*$^{-/-}$-sorted A-T_{RM} cells as previously decribed [43].

RNA-seq. For each population, 1,000 cells were sorted into RLT lysis buffer (Qiagen) containing 1% BME and total RNA purified using the Quick-RNA Microprep kit (Zymo Research). All resulting RNA was used as an input for complementary DNA synthesis using the SMART-Seq v.4 kit (Takara Bio) and 10 cycles of PCR amplification. Next, 1 ng cDNA was converted to a sequencing library using the NexteraXT DNA Library Prep Kit and NexteraXT indexing primers (Illumina) with 10 additional cycles of PCR. Final libraries were pooled at equimolar ratios and sequenced on a HiSeq2500 using 50-bp paired-end sequencing or a NextSeq500 using 75-bp paired-end sequencing. Raw fastq files were mapped to the mm9 build of the mouse genome using Tophat2 (ref. [44]) with the mm9 University of California Santa Cruz KnownGene reference transcriptome[45]. The overlap of reads with exons was computed and summarized using the GenomicRanges[46] package in R/Bioconductor and data normalized to fragments per kilobase per million (FPKM). Genes that were expressed at a minimum of three reads per million (RPM) in all samples for each cell typed were considered to be expressed. DEGs were determined using the glm function in edgeR[47] using the mouse from which each cell type originated as a covariate. Genes with an FDR < 0.05 and absolute $\log_2(FC) > 1$ were considered to be significant. For GSEA[21], all detected genes were ranked by multiplying the sign of the fold change by the $-\log_{10}$ of the *P* value between two cell types. The resulting list was used in a GSEA pre-ranked analysis.

ATAC-seq. For ATAC-seq[24,25], 2,000 cells were isolated by FACS, resuspended in 50 µl of nuclei isolation buffer (10 mM Tris-HCl, pH 7.4, 10 mM NaCl, 3 mM $MgCl_2$, 0.1% IGEPAL CA-630, molecular grade H_2O, filter sterilized), and centrifuged for 30 min at 500*g* and 4 °C. Nuclei were then resuspended in 25 µl of Tagmentation reaction buffer (2X TD buffer, 1 µl of Tagmentation enzyme, molecular grade H_2O (Illumina, Inc.)), incubated for 1 h at 37 °C, and DNA isolated by addition of 25 µl of lysis buffer (326 mM NaCl, 109 mM ethylenediaminetetraacetic acid, 0.63% sodium dodecylsulfate) with incubation for 30 min at 40 °C. Low-molecular-mass DNA was purified by SPRI-bead size selection and PCR amplified using Nextera indexing primer (Illumina) and 2x HiFi ReadyMix (KAPA Biosystems). Final libraries were purified by a second size selection and pooled at equimolar ratio for 50-bp paired-end sequencing on a HiSeq2500. Raw fastq reads were mapped to the mm9 build of the mouse genome using Bowtie[48] with the default settings. For the analysis of accessible regions, the first accessible peaks were identified for each sample using MACS2 (ref. [49]). Second, all unique peaks were merged and the read depth annotated for each sample and normalized to reads per peak using GenomicRanges[46] and R/Bioconductor. DARs were determined using edgeR[47] and those with an FDR < 0.05 and absolute $\log_2(FC) > 1$ were considered to be significant. DARs were annotated to the nearest gene transcription start site using HOMER[50].

Integrative analysis. To integrate the RNA-seq and ATAC-seq data, we used a normalized, Euclidean distance, *k*-means clustering pipeline that we have previously described[26,27]. First, DARs were annotated to the DEGs using the overlap of Entrez ID, resulting in 1,652 DARs mapping to 704 DEGs. Second, for each DAR–DEG combination, data were aggregated by cell type, variance normalized and a pair-wise Euclidean distance matrix calculated. The resulting matrix was *k*-means clustered using a *k* of 3. For each cluster, GO analysis was performed on the DEGs using DAVID[51] and enriched motifs in the DARs were identified with HOMER[50] using the 'findMotifsGenome.pl' script. All other data display was done in R/Bionconductor.

Statistical analysis. Statistical analysis was performed using Prism (GraphPad Software). Each figure legend indicates methods of comparison and corrections.

Reporting Summary. Further information on research design is available in the Nature Research Reporting Summary linked to this article.

Data availability

All sequencing data are available from the National Center for Biotechnology Information Gene Expression Omnibus under accession no. GSE118112. All code, data processing scripts and additional data that support the findings of this study are available from the corresponding author upon request.

References

42. Kohlmeier, J. E. et al. Inflammatory chemokine receptors regulate CD8$^+$ T cell contraction and memory generation following infection. *J. Exp. Med.* **208**, 1621–1634 (2011).
43. Kohlmeier, J. E. et al. The chemokine receptor CCR5 plays a key role in the early memory CD8$^+$ T cell response to respiratory virus infections. *Immunity* **29**, 101–113 (2008).
44. Kim, D. et al. TopHat2: accurate alignment of transcriptomes in the presence of insertions, deletions and gene fusions. *Genome Biol.* **14**, R36 (2013).
45. Hsu, F. et al. The UCSC Known Genes. *Bioinformatics* **22**, 1036–1046 (2006).
46. Lawrence, M. et al. Software for computing and annotating genomic ranges. *PLoS Comput. Biol.* **9**, e1003118 (2013).
47. Robinson, M. D., McCarthy, D. J. & Smyth, G. K. edgeR: a bioconductor package for differential expression analysis of digital gene expression data. *Bioinformatics* **26**, 139–140 (2010).
48. Langmead, B., Trapnell, C., Pop, M. & Salzberg, S. L. Ultrafast and memory-efficient alignment of short DNA sequences to the human genome. *Genome Biol.* **10**, R25 (2009).
49. Zhang, Y. et al. Model-based analysis of ChIP-Seq (MACS). *Genome Biol.* **9**, R137 (2008).
50. Heinz, S. et al. Simple combinations of lineage-determining transcription factors prime *cis*-regulatory elements required for macrophage and B cell identities. *Mol. Cell* **38**, 576–589 (2010).
51. Huang da, W., Sherman, B. T. & Lempicki, R. A. Systematic and integrative analysis of large gene lists using DAVID bioinformatics resources. *Nat. Protoc.* **4**, 44–57 (2009).

Acknowledgements

We thank the New York University Genome Technology Center and University of Albama at Birmingham Helfin Genomics Core for Illumina sequencing, the Emory Integrated Genomics Core for sequencing library Bioanalyzer expertise, Children's Healthcare of Atlanta and Emory University Pediatric Flow Cytometry Core for cell sorting and the NIH Tetramer Core Facility (contract no. HHSN272201300006C). This project was supported by NIH grants (nos. R01HL122559 and R01HL138508) and Centers of Excellence in Influenza Research and Surveillance contracts (no. HHSN272201400004C (to J.E.K.), and nos. 1R01AI113021 and P01AI125180-01 (to J.M.B.)). S.L.H. was supported by an NIH grant (no. F31 HL136101).

Author contributions

S.L.H., C.D.S., J.M.B. and J.E.K. designed the study. S.L.H., C.D.S., E.K.C., Z.-R.T.L. and S.T. performed the experiments. S.L.H., C.D.S., E.K.C., Z.-R.T.L., S.T. and J.E.K. analyzed the data. S.L.H., C.D.S., J.M.B. and J.E.K. wrote the manuscript.

Competing interests

The authors declare no competing interests.

Additional information

Supplementary information is available for this paper at https://doi.org/10.1038/s41590-019-0584-x.

Correspondence and requests for materials should be addressed to J.E.K.

Peer review information I. Visan was the primary editor on this article and managed its editorial process and peer review in collaboration with the rest of the editorial team.

Reprints and permissions information is available at www.nature.com/reprints.

nature research

Corresponding author(s): Jacob E. Kohlmeier

Last updated by author(s): 09/11/2019

Reporting Summary

Nature Research wishes to improve the reproducibility of the work that we publish. This form provides structure for consistency and transparency in reporting. For further information on Nature Research policies, see Authors & Referees and the Editorial Policy Checklist.

Statistics

For all statistical analyses, confirm that the following items are present in the figure legend, table legend, main text, or Methods section.

n/a	Confirmed	
☐	☒	The exact sample size (*n*) for each experimental group/condition, given as a discrete number and unit of measurement
☐	☒	A statement on whether measurements were taken from distinct samples or whether the same sample was measured repeatedly
☐	☒	The statistical test(s) used AND whether they are one- or two-sided *Only common tests should be described solely by name; describe more complex techniques in the Methods section.*
☒	☐	A description of all covariates tested
☐	☒	A description of any assumptions or corrections, such as tests of normality and adjustment for multiple comparisons
☐	☒	A full description of the statistical parameters including central tendency (e.g. means) or other basic estimates (e.g. regression coefficient) AND variation (e.g. standard deviation) or associated estimates of uncertainty (e.g. confidence intervals)
☐	☒	For null hypothesis testing, the test statistic (e.g. *F*, *t*, *r*) with confidence intervals, effect sizes, degrees of freedom and *P* value noted *Give P values as exact values whenever suitable.*
☒	☐	For Bayesian analysis, information on the choice of priors and Markov chain Monte Carlo settings
☒	☐	For hierarchical and complex designs, identification of the appropriate level for tests and full reporting of outcomes
☒	☐	Estimates of effect sizes (e.g. Cohen's *d*, Pearson's *r*), indicating how they were calculated

Our web collection on statistics for biologists contains articles on many of the points above.

Software and code

Policy information about availability of computer code

Data collection	Flow cytometry data collection occurred on either BD LSR II with FacsDiva v6.2 or BD LSRFortessa X-20 with FacsDiva v8.0.1
Data analysis	Flow cytometry data analysis: FlowJo (TreeStar) v10.1 RNA-seq data analysis: Tophat2 v2.0.13, PICARD v1.127, GenomicRanges v1.22.4, edgeR v3.18.1, ATAC-seq data analysis: Bowtie v1.1.1, PICARD v1.127, GenomicRanges v1.22.4, edgeR v3.18.1, HOMER v4.8.2, MACS2 2.1 Other tools: R v3.4.3, vegan v2.4-3, Prism v6

For manuscripts utilizing custom algorithms or software that are central to the research but not yet described in published literature, software must be made available to editors/reviewers. We strongly encourage code deposition in a community repository (e.g. GitHub). See the Nature Research guidelines for submitting code & software for further information.

Data

Policy information about availability of data

All manuscripts must include a data availability statement. This statement should provide the following information, where applicable:

- Accession codes, unique identifiers, or web links for publicly available datasets
- A list of figures that have associated raw data
- A description of any restrictions on data availability

All sequencing data is available from the NCBI Gene Expression Omnibus (GEO) under accession GSE118112. All code and data processing scripts are available upon request.

Field-specific reporting

Please select the one below that is the best fit for your research. If you are not sure, read the appropriate sections before making your selection.

☒ Life sciences ☐ Behavioural & social sciences ☐ Ecological, evolutionary & environmental sciences

For a reference copy of the document with all sections, see nature.com/documents/nr-reporting-summary-flat.pdf

Life sciences study design

All studies must disclose on these points even when the disclosure is negative.

Sample size	No formal sample size power calculations were performed. For mouse phenotyping, an n of 2 or greater and at least 10 mice total per group were used. For genomics assays at least 2 or more samples from independent mice were used as is recommended by the ENCODE Consortium.
Data exclusions	No data was excluded from the analysis.
Replication	All attempts at replication were successful. The ATAC-seq and RNA-seq replication data are reported in a supplemental figure. Where indicated, we validated the differential expression observed by RNA-seq at the protein level by flow cytometry.
Randomization	Samples were grouped by genotype and mice in groups were infected with the same viral isolate. No other randomization was performed.
Blinding	There was no risk of bias in this study from knowing the sample details so blinding was not relevant.

Reporting for specific materials, systems and methods

We require information from authors about some types of materials, experimental systems and methods used in many studies. Here, indicate whether each material, system or method listed is relevant to your study. If you are not sure if a list item applies to your research, read the appropriate section before selecting a response.

Materials & experimental systems

n/a	Involved in the study
☐	☒ Antibodies
☒	☐ Eukaryotic cell lines
☒	☐ Palaeontology
☐	☒ Animals and other organisms
☒	☐ Human research participants
☒	☐ Clinical data

Methods

n/a	Involved in the study
☒	☐ ChIP-seq
☐	☒ Flow cytometry
☒	☐ MRI-based neuroimaging

Antibodies

Antibodies used	CD8a BV785 Clone:53-6.7 Biolegend Cat:100749 Lot:B258589, CD8a BV 510 Clone:53-6.7 Biolegend Cat:100752 Lot:B243669, CD4 BV510 Clone:RM-45 Biolegend Cat:100553 Lot:B260374, CD69 A488 Clone:H1.2F3 Biolegend Cat:104516 Lot:B252252, CD103 BV421 Clone:M290 BD Cat:562771 Lot:8116602, CD103 PerCP Cy 5.5 Clone:2E7 Biolegend Cat:121416 Lot:B252750, CD11a BV510 Clone:M17I4 BD Cat:747760 Lot:9007914, CD11a Superbright 702 Clone:M17I4 Invitrogen Cat:67-0111-82 Lot:2026672, CD44 AF700 Clone:IM7 Ebioscience Cat:56-0441-82 Lot:1980496, CD44 BV510 Clone:IM7 Biolegend Cat:103043 Lot:B258590, CD62L BV605 Clone:MEL-14 Biolegend Cat:104437 Lot:B249676, Zombie NIR Biolegend Cat:77184 Lot:B285743, 7AAD Biolegend Cat:420404 Lot:B287621, CD3e PeCF-594 Clone:145-2C11 BD Cat:562286 Lot:8199538, CD45.2 PE Clone:104 Biolegend Cat:109808 Lot:B258822, CD45.2 BV421 Clone:104 Biolegend Cat:109832 Lot:B250136,CD98 PE Clone:RL388 Biolegend Cat:128208 Lot:B212621, CD98 A647 Clone:RL388 Biolegend Cat:128210 Lot:B223425, CXCR3 PerCP Cy 5.5 Clone:CXCR3-173 Biolegend Cat:126514 Lot:B166846, CD45.1 BUV737 A20 BD Cat:612811, Annexin V Biolegend Cat:640943 Lot:B263822, BCL2 PE Clone:3F11 BD Cat:556537
Validation	All antibodies used came from commercial vendors as specified above. Specificity was based their provided description and data sheets, and previously published clones and flurochromes. Validation was provided by example staining on manufacturers website and additional validation came from references provided by each manufacturer

Animals and other organisms

Policy information about studies involving animals; ARRIVE guidelines recommended for reporting animal research

Laboratory animals	C57BL/6J (WT), B6.SJL-Ptprca Pepcb/BoyJ (CD45.1), and B6.129S(Cg)-Ddit3tm2.1Dron/J (Ddit3-/-) mice were purchased from The

Laboratory animals	Jackson Laboratory. C57BL/6J were crossed with B6.SJL-Ptprca Pepcb/BoyJ in house to provide CD45.1/CD45.2 congenic WT hosts for various purposes. Mice were a combination of male and female based on availability.
Wild animals	This study did not involve wild animals.
Field-collected samples	The study did not involve field-collected samples.
Ethics oversight	All experiments were completed in accordance with the Institutional Animal Care and Use Committee guidelines of Emory University and Kindai University.

Note that full information on the approval of the study protocol must also be provided in the manuscript.

Flow Cytometry

Plots

Confirm that:

☒ The axis labels state the marker and fluorochrome used (e.g. CD4-FITC).

☒ The axis scales are clearly visible. Include numbers along axes only for bottom left plot of group (a 'group' is an analysis of identical markers).

☒ All plots are contour plots with outliers or pseudocolor plots.

☐ A numerical value for number of cells or percentage (with statistics) is provided.

Methodology

Sample preparation	A description of the sample preparations for flow cytometry and sorting is detailed in the Methods section.
Instrument	Flow cytometry data collection occurred on either BD LSR II or BD LSRFortessa X-20. Sorts were performed on a BD Aria II
Software	Flow cytometry data collection occurred on either BD LSR II with FacsDiva v6.2 or BD LSRFortessa X-20 with FacsDiva v8.0.1. Analysis of data sets was performed with FlowJo v10 software.
Cell population abundance	Test sorting on influenza specific T cell populations yielded greater 98% purity
Gating strategy	All samples were pre-gated using the following strategy: 1) Singlets based on FSC-H/FSC-W, then SSC-H/SSC-W; 2) Lymphocytes based on FSC-A/SSC-A; 3) Live cells based on L/D Zombie NIR negative or 7AAD; 4) CD4- CD8+ 5) For Lung intersitium population and BAL, cells were gated on IV antibody negative; 6) Cells were gated on Tetramer positive by CD44 positive; 7)Cells were further gated on populations of interest. Additionally for sorting for RNA seq for populations which were sorted on bulk CD44 high we continue through step 5, then cell are gated on CD44 high CD62L low before isolation.

☐ Tick this box to confirm that a figure exemplifying the gating strategy is provided in the Supplementary Information.